Electronic Supplementary Information to: Stochastic microstructure modeling of SOC electrodes based on a pluri-Gaussian approach

Philip Marmet,*[a,c] Lorenz Holzer,[a] Thomas Hocker,[a] Vinzenz Muser,[a] Gernot K. Boiger,[a] Mathias Fingerle,[b] Sarah Reeb,[b] Dominik Michel,[b] and Joseph M. Brader[c]

[a] *Zurich University of Applied Sciences, Institute of Computational Physics, CH-8400 Winterthur, Switzerland. E-mail: mame@zhaw.ch*
[b] *Math2Market GmbH, D-67657 Kaiserslautern, Germany.*
[c] *Department of Physics, University of Fribourg, CH-1700 Fribourg, Switzerland.*

Contents

A Noise-filtering at the interfaces of the phases

A known issue of the PGM (e.g.,[1]) is that the thresholding of the Gaussian random fields result in an irrelevant noise at the interfaces of the phases as illustrated in Fig. 1 a). Therefore, an option is implemented to filter the Gaussian random fields with a low-pass Gaussian filter in order to suppress these interface artefacts as e.g., suggested by Abdallah et al.[1]. The standard deviation of the Gaussian filter is specified as a fraction of the standard deviation of the Gaussian random field, which enables the use of standard values independent of the characteristic phase size and resolution:

$$k_{\mathrm{Filter}} = \frac{SD_{\mathrm{Filter}}}{SD_{\mathrm{GRF}}} \tag{1}$$

where SD_{GRF} is the standard deviation of the Gaussian random field and SD_{Filter} the standard deviation of the Gaussian filter. Suitable default values are determined with a sensitivity analysis reported in section A.1. As there is no absolute reference for the 'true' interface area, the filter parameters are chosen with the aim to achieve the same interface areas independent of the characteristic phase size and resolution. The study suggests that a filter factor $k_{\mathrm{Filter}} = 0.025$ is a good choice. Fig. 1 b) shows an example with this filter settings, where the noise at the interfaces is suppressed but still all the features are resolved. A too strong filtering results in a suppression of small structure features as shown in Fig. 1 c). The Gaussian filter is especially important, if one of the solid phases is described with a Gaussian random field with a standard deviation SD_{GRF} above 10 voxels. Moreover, the study shows that the volume specific interface area is systematically lower for low resolutions (i.e., low SD_{GRF}) because not all the features can be sufficiently resolved. A minimal standard deviation of $SD_{\mathrm{GRF}} = 10$ voxels for the Gaussian random fields thus seems to be a good compromise between sufficient resolution and needed structure size in order to get a representative elementary volume (REV) with reasonable computational effort.

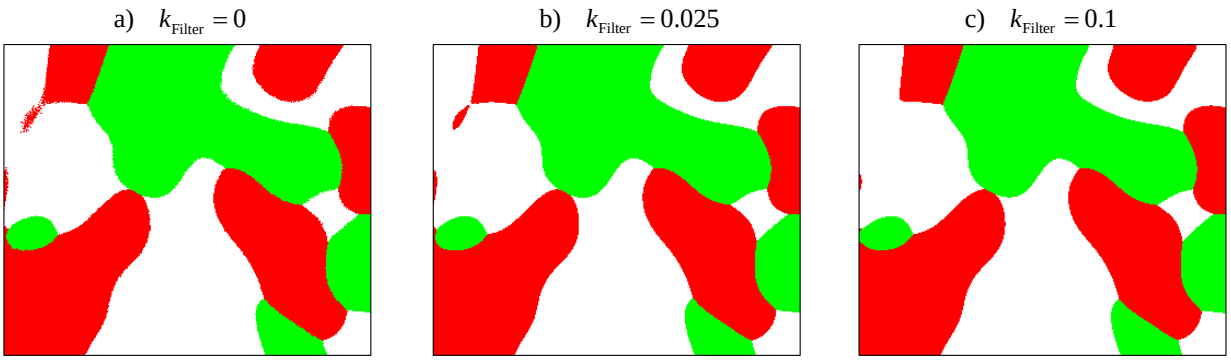

Fig. 1 Illustration of the noise-filtering at the interfaces of the phases for a structure with a standard deviation of the Gaussian random field of 40 voxels for both solid phases: a) No filter operation applied: irrelevant noise at the phase interfaces is clearly visible, b) Gaussian filter with $k_{\mathrm{Filter}} = 0.025$ (optimized): irrelevant noise at the phase interfaces is removed and all features are preserved and c) Gaussian filter with $k_{\mathrm{Filter}} = 0.1$: irrelevant noise at the phase interfaces is removed but some features already vanished, which shows that the filter factor is too large.

A.1 Sensitivity analysis for the noise-filtering at the interfaces of the phases

A Gaussian filter is applied on the gaussian random field in order to suppress irrelevant noise at the interfaces of the phases as introduced in section A. In this section, a sensitivity analysis is performed in order to provide appropriate default values for the filter parameters of the Gaussian filter. In Fig. 2, orthoslices of the 3D-structures for different standard deviations (SD) of the gaussian random fields without filter operations for a total solid volume fraction $\phi_{\mathrm{tot}} = 50\,\%$ and equal volume fractions for the two solid phases are presented. The voxel size is adapted accordingly in order to represent the same characteristic phase size for all the structures. For all the structures, a structure size of 600^3 voxels and a neutral wetting behaviour was used. For SD = 5 voxels and SD = 10 voxels, no artefacts are visible at the interfaces of the phases. Starting from SD = 20

voxels, irrelevant noise is visible at the interfaces. The noise level further increases for SD = 30 and SD = 40 voxels.

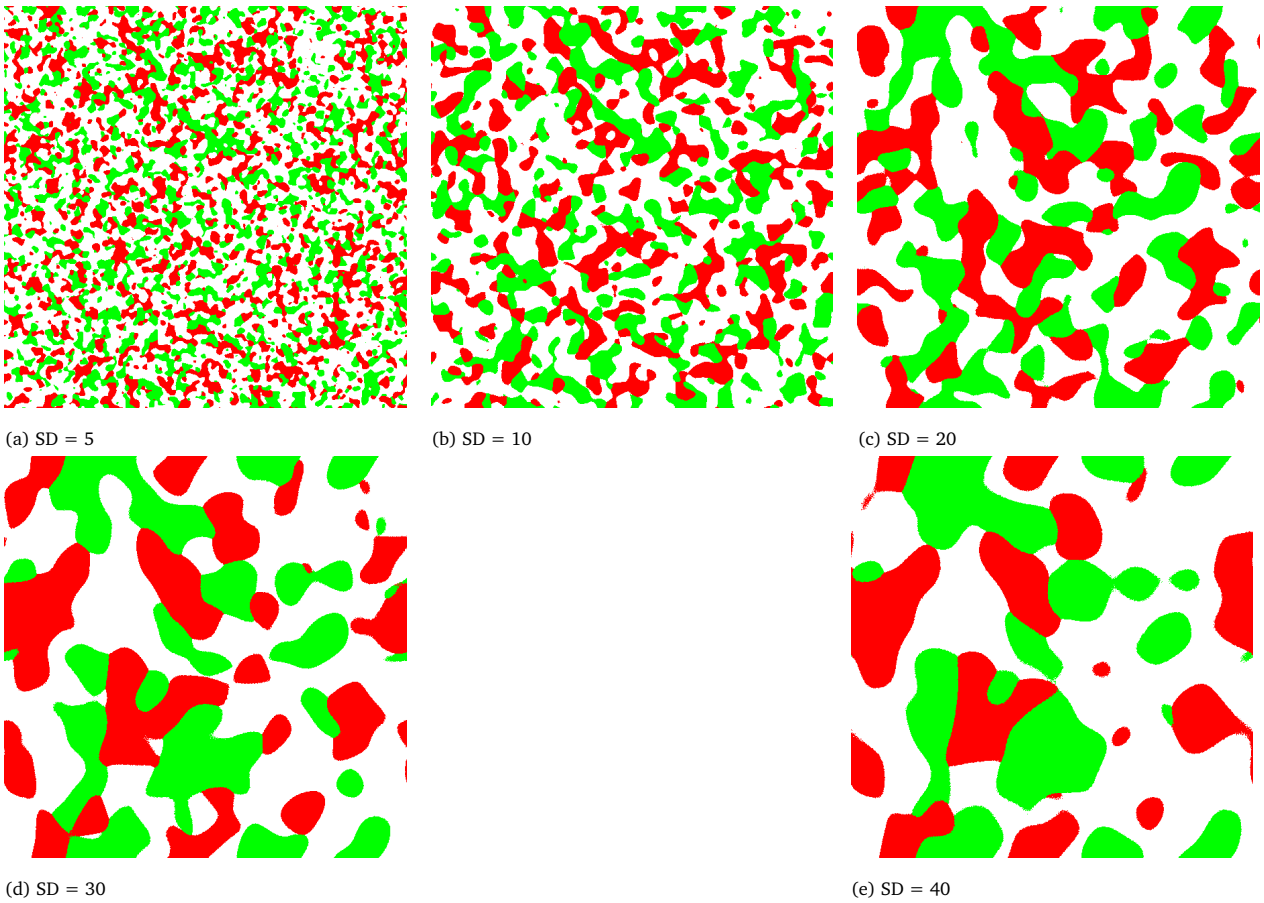

(a) SD = 5 (b) SD = 10 (c) SD = 20

(d) SD = 30 (e) SD = 40

Fig. 2 Orthoslices of the 3D-structures for different standard deviations (SD) of the gaussian random fields without filter operations for a total solid volume fraction of $\phi_{tot} = 50\,\%$. For all the structures, a structure size of 600^3 voxels and a neutral wetting behaviour (i.e., $\alpha = 45°$, $\beta = 0°$, $\gamma = 0°$) was used. For higher standard deviations with SD $\geq$ 20 voxels (i.e., higher resolution), artefacts can be observed at the interfaces between the phases.

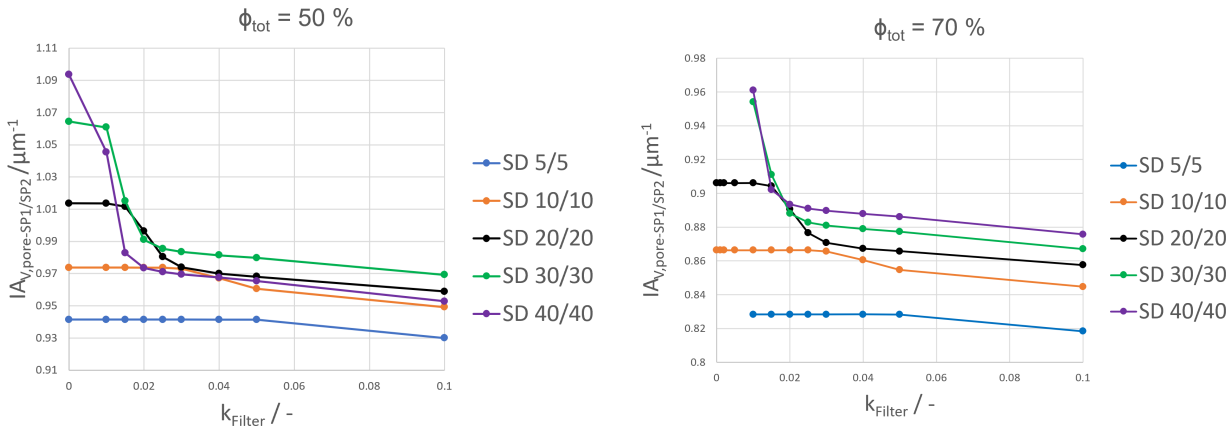

(a) $\phi_{tot} = 50\,\%$ (b) $\phi_{tot} = 70\,\%$

Fig. 3 Volume specific pore-SP1/SP2 interface area (averaged value for pore-SP1 and pore-SP2) for different standard deviations (SD) for the Gaussian random fields as a function of the Gauss filter factor k_{Filter} for a) a total solid volume fraction $\phi_{tot} = 50\,\%$ and b) for a total solid volume fraction $\phi_{tot} = 70\,\%$. For all the structures, a structure size of 600^3 voxels and a neutral wetting behaviour was used.

In Fig. 3, the volume specific pore-SP1/SP2 interface areas are plotted for different standard deviations (SD) of the gaussian random fields as a function of the Gauss filter factor k_{Filter} for a) a total solid volume fraction $\phi_{\mathrm{tot}} = 50\,\%$ and b) for a total solid volume fraction $\phi_{\mathrm{tot}} = 70\,\%$. For all the structures, a structure size of 600^3 voxels and a neutral wetting behaviour was used. Note that the volume specific interface area pore-SP1 and pore/SP2 are expected to be equal because of the equal phase volume fraction neutral wetting behaviour and are therefore averaged in order to get a better statistic. The visual impression for the noise at the interfaces of the orthoslices in Fig. 2 is confirmed by the values of the volume specific interface areas in Fig. 3 a) with $k_{\mathrm{Filter}} = 0$, showing an increasing interface area for increasing SDs. With an increasing filter-factor, the structures with SD=20/30/40 voxels show a steep decrease in the interface area after a certain threshold, followed by an almost linear and smaller decrease. For the structures with SD=5/10 voxels, to first section with a steep decrease of the interface area is not present and the curves directly start with the less steep and almost linear evolution. A filter factor of $k_{\mathrm{Filter}} = 0.025$ thereby seems to be a good choice for a default value, as the values for the filter areas for SD=10/20/30/40 voxels are very close. However, the interface area for a SD = 5 voxels is considerably lower, because the smaller features are no more fully resolved because of the insufficient resolution. This trend is even clearer for the dataset with $\phi_{\mathrm{tot}} = 70\,\%$ in Fig. 3 b), showing a systematically higher interface area for higher SDs because of the better resolution of the small features. However, a standard deviation of 10 voxels for the Gaussian random fields seems to be a good compromise between sufficient resolution and needed structure size in order to get a representative elementary volume (REV) with reasonable computational effort.

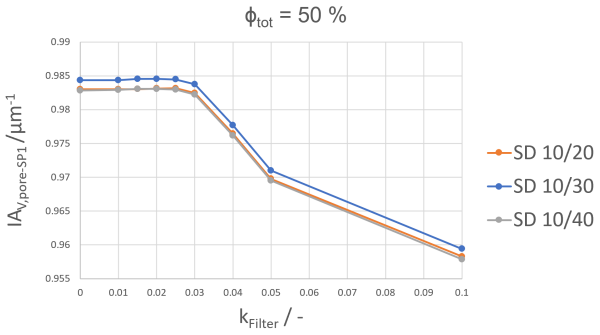

(a) Volume specific interface area pore-SP1 for $\phi_{\mathrm{tot}} = 50\,\%$.

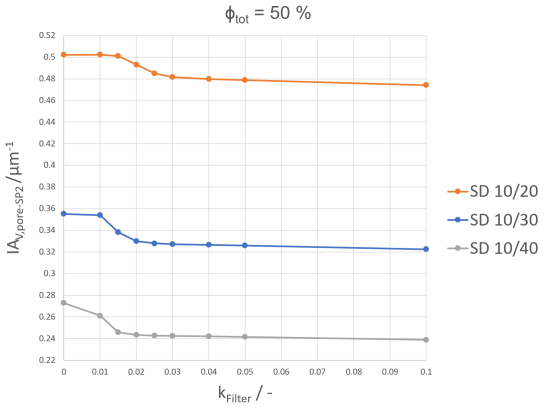

(b) Volume specific interface area pore-SP2 for $\phi_{\mathrm{tot}} = 50\,\%$.

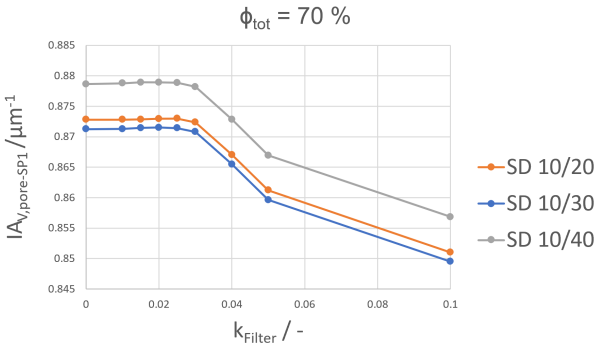

(c) Volume specific interface area pore-SP1 for $\phi_{\mathrm{tot}} = 70\,\%$.

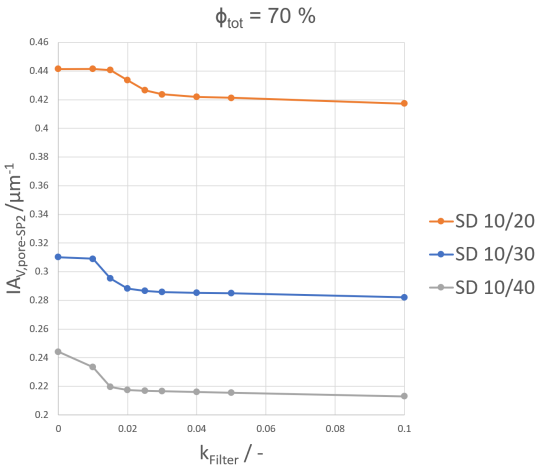

(d) Volume specific interface area pore-SP2 for $\phi_{\mathrm{tot}} = 70\,\%$.

Fig. 4 Volume specific interface areas for structures with different characteristic lengths (i.e., standard deviations of the Gaussian random fields) for a total solid volume fraction $\phi_{\mathrm{tot}} = 50\,\%$ (a),b)) and for a total solid volume fraction $\phi_{\mathrm{tot}} = 70\,\%$ (c),d)).

The noise filtering at the interfaces is especially relevant, if different characteristic sizes shall be modelled for the two solid phases in order to get consistent interface areas. This important case is tested with a further sensitivity analysis for the volume specific interface areas as a function of the filter factor reported in Fig. 4. Thereby, SP1 is held constant and resolved with an SD = 10 voxels, while larger characteristic sizes are used for SP2. Moreover, structures with $\phi_{\text{tot}} = 50\,\%$ and $\phi_{\text{tot}} = 70\,\%$ are tested. Consequently, the volume specific interface areas for pore-SP1 (Fig. 4 a) and c)) are always in the same range, while the volume specific interface areas for pore-SP2 (Fig. 4 b) and d)) differ for the different structures according to the chosen characteristic sizes. The course of the interface areas again confirm that a filter factor of $k_{\text{Filter}} = 0.025$ is a good default value. The orthoslices of the corresponding 3D structures for a filter factor of $k_{\text{Filter}} = 0.025$ are reported in Fig. 5. The visual inspection confirms the successful suppression of the noise at the interfaces of the phases even for different characteristic sizes of the solid phases. Note that the inclusions of the green phase (SP1) in the red phase (SP2 with the larger characteristic size) is characteristic for the chosen neutral wetting and might be varied by different settings of the threshold angles α, β and γ.

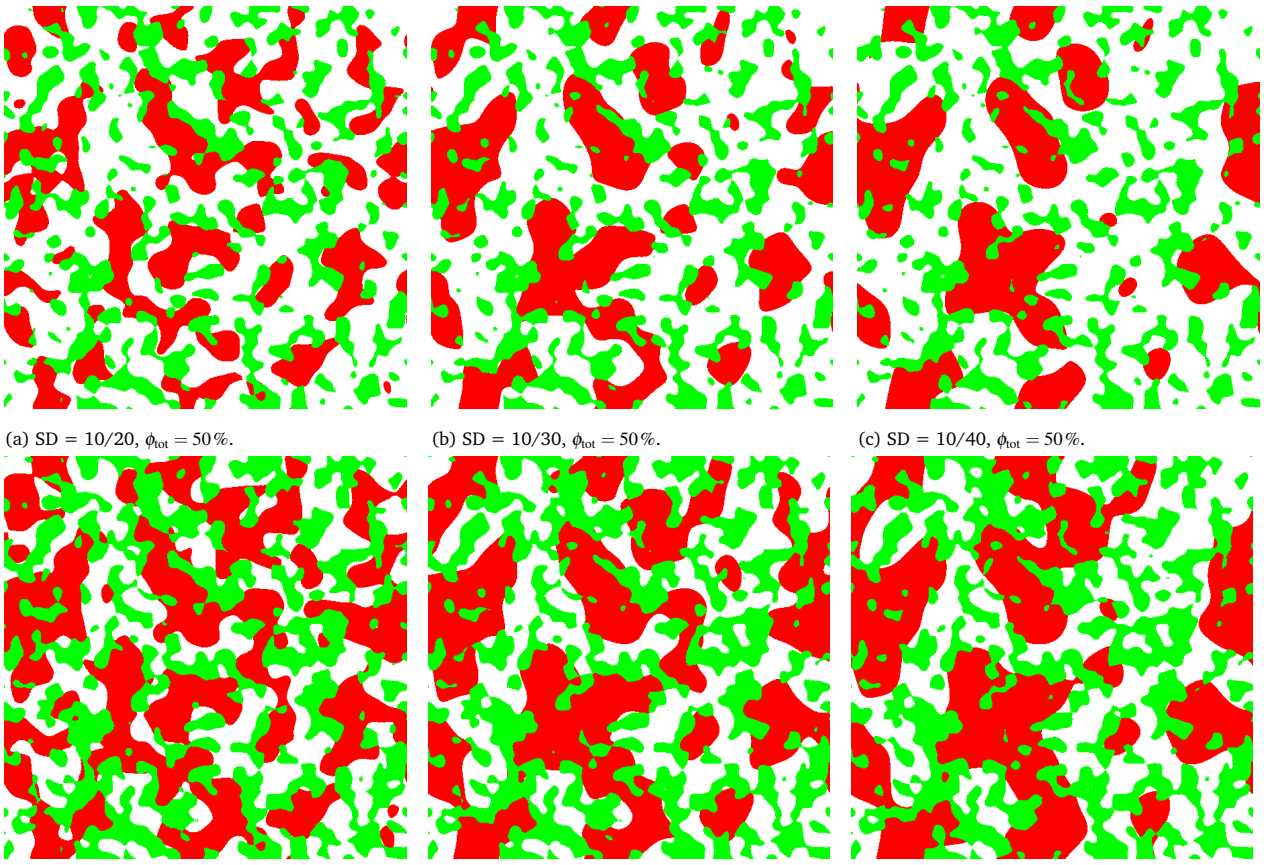

(a) SD = 10/20, $\phi_{\text{tot}} = 50\,\%$. (b) SD = 10/30, $\phi_{\text{tot}} = 50\,\%$. (c) SD = 10/40, $\phi_{\text{tot}} = 50\,\%$.

(d) SD = 10/20, $\phi_{\text{tot}} = 70\,\%$. (e) SD = 10/30, $\phi_{\text{tot}} = 70\,\%$. (f) SD = 10/40, $\phi_{\text{tot}} = 70\,\%$.

Fig. 5 Orthoslices of the 3D-structures using a filter factor of $k_{\text{Filter}} = 0.025$ for different characteristic sizes of the two solid phases, for a total solid volume fraction $\phi_{\text{tot}} = 50\,\%$ (a)-c)) and for a total solid volume fraction $\phi_{\text{tot}} = 70\,\%$ (d)-f)).

B PGM-app for stochastic microstructure modeling of SOC electrodes

In the main article, the stochastic modeling of SOFC-electrodes based on a pluri-Gaussian approach has been reported. For the structure generation with the pluri-Gaussian method, a Python app has been developed which can be executed in the GeoDict software-package. The graphical user interface (GUI) of this app is shown in Fig. 6 and some typical parameters are reported in the fields. Note that these parameters are not exactly the default parameters of the PGM-app (specifically, the number of voxels in the fields 1-3 are 200 voxels and the tolerance for the solid volume fractions is 0.01 vol.% by default). However, the default

parameters for the PGM-app are chosen in order to generate a test structure in a short time, for which a representative elementary volume (REV) is not reached. Parameter studies for appropriate parameters for an accurate representation of a microstructure are reported in section D. The settings and parameters for the configuration of the PGM-app are described in the following.

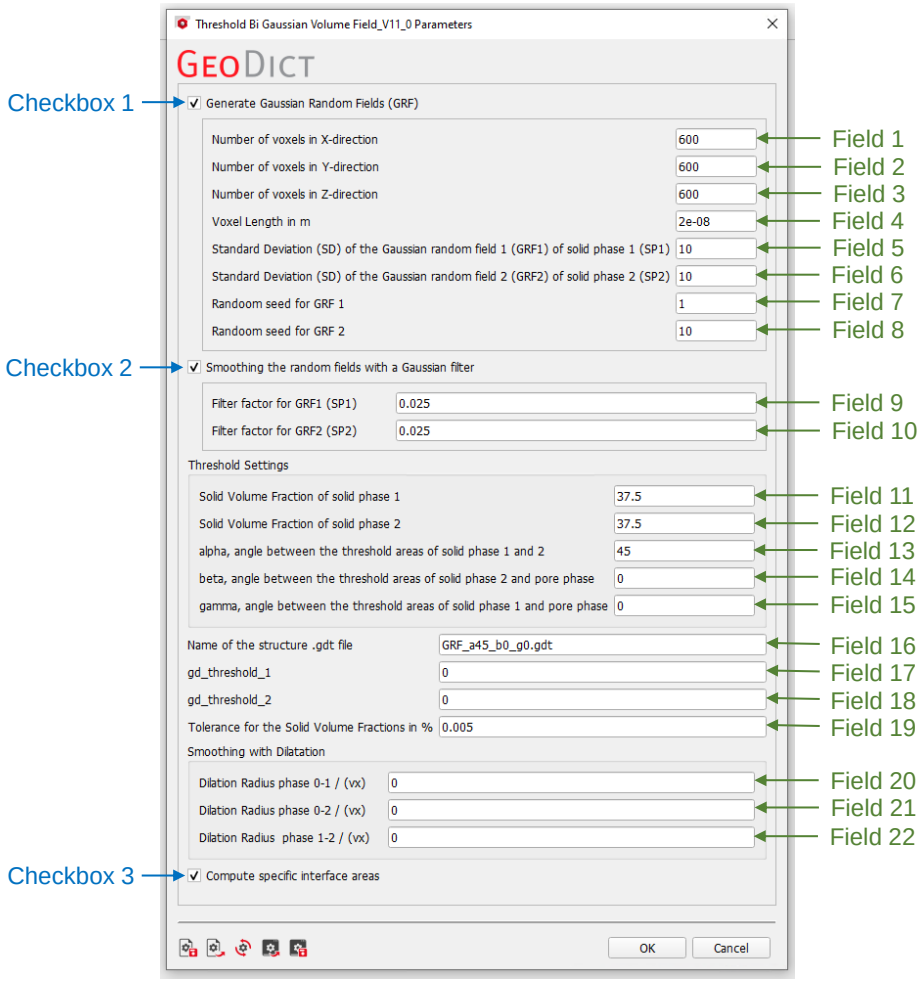

Fig. 6 Python app for the structure generation with the pluri-Gaussian method (PGM-app), which can be executed in GeoDict.

Checkbox 1 enables or disables the generation of a new set of two Gaussian random fields. This checkbox needs to be enabled for the first run. For further runs, the checkbox can be disabled, if the same set of two Gaussian random fields shall be used with different threshold settings for the next structure. The fields of the checkbox group 1 correspond to the parameters described in table 1 in section 2.2 of the main article. Note that a standard deviation of 10 voxels for the Gaussian random fields (field 5 and 6) in combination with the structure size of 600^3 voxels (fields 1-3) are a good compromise between accuracy and computation time. For an appropriate microstructure representation, a sufficient resolution and sufficient structure size for a representative elementary volume (REV) needs to be ensured. If the value for the standard deviation is chosen considerably below 10 voxels, some features can no more be fully resolved, which for example results in too small volume specific interface areas or an insufficient description of the bottlenecks. For very different standard deviations for the two Gaussian random fields, often some compromises for the accuracy need to be made to limit the needed computation time. A sufficient REV is especially critical for the transport properties

(i.e., conductivity, diffusivity, permeability etc.) and for low phase volume fractions of the transporting phases. Parameter studies to achieve an REV are reported in section D. In field 4, the voxel length can be specified. As the standard deviation for the Gaussian random fields (fields 5 and 6) are specified in voxels, a change of the voxel length does also change the characteristic size of the phases.

Checkbox 2 enables or disables the smoothing of the Gaussian random fields as described in section A. Note that the filter parameters (fields 9 and 10) are defined relative to the standard deviation for the Gaussian random fields (fields 5 and 6) and do not need to be adapted for different standard deviations or voxel length (field 4). The standard values of 0.025 are thus a good choice for almost all cases and there is no need to adapt them in general.

The threshold settings group (fields 11-19) define the thresholding of the set of two Gaussian random fields in order to obtain a three-phase structure (two solid-phases and one pore-phase) as reported in table 2 and explained in section 2.2 of the main article. The fields 11 and 12 define the volume fractions of the two solid-phases, while the volume fraction of the pore-phase is simply the remaining space. The thresholding angles in the fields 13-15 define the wetting behaviour of the phases. The definition of the angles is illustrated in Fig. 4 of the main article. Note that there are some restrictions for the combinations of the angles α, β and γ, as a minimal angle for the domains for SP1, SP2 and the pore-phase needs to be ensured. Specifically, the following relations need to be fulfilled.

- Domain SP1: $90^\circ + \alpha - \gamma > 20^\circ$
- Domain SP2: $180^\circ + \beta - \alpha > 20^\circ$
- Domain pore-phase: $90^\circ - \beta + \gamma > 20^\circ$
- General: $0^\circ \leq \alpha \leq 90^\circ$, $-90^\circ \leq \beta \leq 40^\circ$ and $-40^\circ \leq \gamma \leq 90^\circ$

Note that the limit of 20° is not strict. Zone values of 10° or even below will work as well for the PGM-app. However, many iterations and therewith longer computation times are expected. Moreover, these extreme cases are often of limited interest for the application. In field 19, the tolerance for the phase volume fractions is defined in vol.%. The thresholding iterations are stopped as soon as this tolerance is reached for both solid phases, but latest after 100 iterations. In field 16, the name of the structure can be defined. Note that this name needs to be changed in every run, as otherwise the structure of the last run will be overwritten. The parameters of the fields 17 and 18 represent the initial thresholding parameters TH_1 and TH_2 visualized in Fig. 4 of the main article and are for debugging purposes only.

The smoothing with dilatation group (fields 20-22) is another possibility for the smoothing of the structure at the end of the construction process using morphological operations. The drawback of this technique is that it causes some deviations for the phase volume fractions. Thus, the smoothing of the Gaussian random fields (checkbox 2) is recommended for general purposes.

With checkbox 3, the computation of the volume specific interface areas can be enabled or disabled. The determination of these properties is quite fast and often useful for a first interpretation of the realized virtual microstructure. However, for a detailed characterization, the characterization-app reported in a previous publication[2] can be used.

After the generation of the microstructure, the input parameters, the achieved solid phase volume fractions and if selected the volume specific interface areas are reported in a csv-file. An example of this report-file is reported in Fig. 7 for the parameters used in Fig. 6. The standard deviation for the Gaussian filter (sigma_ GaussFilter_SP1 and sigma_GaussFilter_SP2) are reported in absolut voxel values and correspond to 2.5 % of the standard deviations for the Gaussian random field. The deviations of the realized solid volume fractions is below 0.005 vol.% as requested in the settings. The reported volume specific interface areas IA_V_pore-SP1 and IA_V_pore-SP2 should theoretically be identical for the chosen input parameters. In fact, they differ about 0.2 %, which confirms that the chosen structure size of 600^3 voxels is sufficient, at least concerning the volume specific interface areas.

Description	Variable	Unit	Value
Name of the structure-file	StructureName	-	GRF_a45_b0_g0.gdt
Number of voxels in X-direction	NX	vox	600
Number of voxels in Y-direction	NY	vox	600
Number of voxels in Z-direction	NZ	vox	600
Voxel length	VoxelLength	nm	20
Standard deviation of the Gaussfield of solid phase 1	StandardDeviation_SP1	vox	10
Standard deviation of the Gaussfield of solid phase 2	StandardDeviation_SP2	vox	10
Random seed for the GRF of solid phase 1	RandomSeed_GRF1	-	1
Random seed for the GRF of solid phase 2	RandomSeed_GRF2	-	10
Predefined solid volume fraction of solid phase 1	SVF_SP1_def	%	37.5
Predefined solid volume fraction of solid phase 2	SVF_SP2_def	%	37.5
Tolerance for the solid volume fractions	SVF_Tolerance	%	0.005
Angle between the threshold areas of solid phase 1 and 2	alpha	°	45
Angle between the threshold areas of solid phase 2 and pore phase	beta	°	0
Angle between the threshold areas of solid phase 1 and pore phase	gamma	°	0
Dilation radius phase 0-1	DilationRadius_0_1	vox	0
Dilation radius phase 0-2	DilationRadius_0_2	vox	0
Dilation radius phase 1-2	DilationRadius_1_2	vox	0
Standard deviation for the Gaussian filter for SP1	sigma_GaussFilter_SP1	vox	0.25
Standard deviation for the Gaussian filter for SP2	sigma_GaussFilter_SP2	vox	0.25
Realized solid volume fraction of solid phase 1	SVF_SP1	%	37.49979815
Realized solid volume fraction of solid phase 2	SVF_SP2	%	37.50476389
Realized total porosity	Epsilon_tot	%	24.99543796
Realized threshold 1 to achieve the defined volume fractions	threshold_1	%	-0.002889639
Realized threshold 2 to achieve the defined volume fractions	threshold_2	%	0.002647694
Volume specific interface area pore phase - solid phase 1	IA_V_pore-SP1	mu^2/mu^3	1.587906608
Volume specific interface area pore phase - solid phase 2	IA_V_pore-SP2	mu^2/mu^3	1.590729242
Ratio volume specific interface area pore phase - solid phase 1 / 2	R_IA_pore-SP1/IA_pore-SP2	mu^2/mu^3	0.998225572
Volume specific surface area of pores	S_V_pore	mu^2/mu^3	3.17863585
Volume specific interface area solid phase 1 - solid phase 2	IA_V_SP1-SP2	mu^2/mu^3	1.626188931

Fig. 7 Construction report for the structure generation with the pluri-Gaussian method.

C Comparison of the computation times for the structure generation with GrainGeo and PGM

In this section, the computation times needed for the structure generation with the PGM approach shall be compared with those needed for the reference sphere-packing structures reported in a previous publication[2]. The three sphere-packing structures were generated using the GrainGeo module within the commercial GeoDict software-package[3]. The corresponding construction times are reported in column a) of table 1. A large increase of the computation time is observed for decreasing porosities, because more spheres have to be packed into the domain by the GrainGeo algorithm. The computation time for a porosity of 20 % is by a factor of 20 higher than for a porosity of 50 %. Three corresponding PGM structures with the same size of 600^3 voxels and equal phase volume fractions are constructed for a fair comparison of the computation times. Moreover, the same workstation was used for all the tests. As the PGM structure generation times depend on the threshold settings, the computation times of two wetting behaviours with neutral wetting (NW) and with a wetting behaviour where SP2 wets SP1 are reported in the columns b) and d) of table 1, respectively. Moreover, the two Gaussian random fields (GRF) can be reused for all the PGM structures. Thus, the computation times are also reported for the thresholding operations only for the two wetting behaviours in the columns c) and e) of table 1, respectively. For all the PGM structures, the generation of the GRFs is more time consuming than the thresholding operations. Thus, the option to reuse the GRFs is very favourable if this is possible for a specific parameter study. The thresholding operations are by a factor of about two more time consuming for the more complex wetting behaviour (SP2 wets SP1) compared to the simple NW case. Moreover, there is a small increase of the computation time with increasing porosity, because of the initial threshold settings at the start of the thresholding iterations. However, this small variation in the range of a factor of 1.3 is negligible compared to the variation of the computation times by a factor of about 20 for the sphere-packing structures. Generally, the computation times are between 1-2 orders of magnitude lower for the PGM structures compared to the sphere-packing structures. For the set of three structures, a computation time of 11.75 hours is needed for the sphere-packing structures but only about 7 minutes or 11 minutes for

the two wetting behaviours for the PGM structures (for the case that the GRFs are only generated ones per set). Thus, for the used set of three sample structures, the computation times are by a factor of 103 (or by a factor of 65 for the more complex wetting behaviour) lower for the PGM approach compared to the sphere-packing approach using GrainGeo. These results clearly illustrate the advantage of the PGM approach in terms of computation times. For the PGM-approach, there is even further potential for a reduction of the computation time as discussed in section 2.2 of the main article. Moreover, the PGM approach also provides a more realistic description of SOC microstructure, as discussed in section 1 of the main article.

Table 1 Comparison of the computation times for the structure generation with PGM and the GrainGeo module of GeoDict. All the generated structures have a size of 600^3 voxels. The computation times are compared for different phase volume fractions. For the computation times without GRF construction (thresholding only), the GRFs of a previous run were reused. NW corresponds to a neutral wetting behaviour using $\alpha = 45°$, $\beta = 0°$ and $\gamma = 0°$. The term "wetting" refers to a wetting behaviour where SP2 wets SP1 using $\alpha = 80°$, $\beta = -40°$ and $\gamma = 0°$.

Structure	a) sphere-packing (GrainGeo)	b) PGM NW full constr.	c) PGM NW only thresholding	d) PGM "wetting" full constr.	e) PGM "wetting" only thresholding
SP1:SP2:pore = 40:40:20	521.2 min = 8.69 h	4.24 min	1.08 min	5.59 min	2.43 min
SP1:SP2:pore = 40:30:30	158.2 min = 2.64 h	4.37 min	1.21 min	5.65 min	2.50 min
SP1:SP2:pore = 30:20:50	25.4 min = 0.42 h	4.54 min	1.39 min	5.96 min	2.80 min

D Parameter study for the pluri-Gaussian structures to ensure a representative elementary volume (REV)

	Reference					
Standard deviation (STDV) of the Gaussian random fields	**10**	**30**	**20**	**20**	**5**	**5**
Porosity	30%	30%	30%	30%	30%	30%
Solid volume fraction SP1	35%	35%	35%	35%	35%	35%
Solid volume fraction SP2	35%	35%	35%	35%	35%	35%
Structure size / vox	800	900	600	600	600	600
Random seed for the GRF of solid phase 1	1	1	1	2	1	2
Random seed for the GRF of solid phase 2	10	10	10	9	10	9
Mean relative conductivity (M-factor) averaged for SP1 / SP2	0.1179	0.1256	0.1284	0.1261	0.1121	0.1108
Difference relative conductivity (M-factor) (SP1-SP2)/SP1	0.77%	-2.91%	-1.06%	10.69%	0.07%	-0.35%
Difference relative conductivity (M-factor) to reference STDV = 10, 800 vox	-	6.52%	8.96%	7.02%	-4.91%	-6.00%

Fig. 8 Parameter study for the standard deviation of the Gaussian random fields (i.e., resolution).

In this section, suitable parameters for the PGM-structure shall be determined in order to achieve a sufficient resolution of the structure features and at the same time ensure a representative elementary volume (REV) of the virtual structure.

In Fig. 8, a variation of the standard deviation of the Gaussian random fields and therewith the resolution of the structure features is reported. To capture the uncertainty of the stochastic realization, also the random seeds for the Gaussian random fields are varied. The relative conductivity rises significantly (around 10 %), if the resolution is changed from 10 to 20 voxels standard deviation (STDV). This is probably at least partially because of the better resolution of the bottlenecks. For an even higher resolution of 30 voxels STDV, the relative conductivity does not rise anymore. For a lower resolution of 5 voxels STDV, the relative conductivity decrease (-5 % and -6 % for the two realizations), probably mainly because of the worse resolution of the bottlenecks. However, there is also a tendency of a decreasing relative conductivity for larger structure sizes (for the same resolution), as observed in the corresponding study reported in Fig. 9. Thus, a part of the change might be due to the lower structure size used compared to the study with STDV = 10 vox. In sum, the resolution of 10 voxels STDV is a good compromise between accuracy and computation time and underestimates the relative conductivity systematically for about 5 %. However, the relative deviation between two parameter variations is typically below 2 % and therewith much lower.

	Reference					
# of voxels	800	600	500	400	300	200
Porosity	30%	30%	30%	30%	30%	30%
Solid volume fraction SP1	35%	35%	35%	35%	35%	35%
Solid volume fraction SP2	35%	35%	35%	35%	35%	35%
Mean relative conductivity (M-factor) averaged for SP1 / SP2	0.1179	0.1230	0.1227	0.1221	0.1258	0.1311
Difference relative conductivity (M-factor) (SP1-SP2)/SP1	0.77%	0.08%	-4.52%	-3.88%	5.77%	29.08%
Difference relative conductivity (M-factor) to reference 800 vox	-	4.31%	4.09%	3.61%	6.70%	11.25%
Volume specific TPB-length	13.516	13.626	13.750	13.652	14.155	13.991
Difference volume specific TPB-length to reference 800 vox		0.82%	1.73%	1.01%	4.73%	3.52%
Volume specific interface area pore-SP1	1.709	1.734	1.722	1.718	1.723	1.653
Difference volume specific interface area (pore-SP1 - pore-SP2) / pore-SP1	0.34%	-0.14%	0.08%	0.42%	2.61%	5.84%
Deviation of the volume specific inerface area pore-SP1 to reference 800 vox		1.46%	0.74%	0.54%	0.81%	-3.28%

Fig. 9 Parameter study for the pluri-Gaussian structures to determine the needed structure size to reach a representative elementary volume (REV). Structures with standard deviations of the Gaussian random fields of 10 voxels and a porosity $\varepsilon = 30\,\%$ were used.

The structure size for the PGM structures is varied in order to determine the needed structure size to obtain an REV. The most important metrics are calculated for different cubic structure sizes (number of voxels) and are reported in Fig. 9. For the volume specific interface areas and the TPB-length, a structure size of 400^3 voxels is sufficient to limit the variation of the metrics to about 1 %. However, the relative conductivities are more sensitive to the structure size. A good measure is the deviation of the conductivities of the two solid phases, as they are theoretically equal for the used structures with the same solid-phase volume fractions and neutral wetting behaviour. Moreover, the self-consistency is more important for our studies than the absolute numbers. This deviation is below 1 % for structure size of 800^3 and 600^3 voxels and rises significantly for structure sizes below 600^3 voxels. However, there is a deviation of about 5 % of the absolute value of the conductivity for the voxel sizes 400^3-600^3 voxels compared to the 800^3 voxels structure, which is acceptable for our studies in order to limit the computational effort. Note that these are statistical results and a single realisation cannot provide reliable information about the accuracy. Therefore, the calculations are repeated for different random seeds for the structure sizes of 500^3 and 600^3 voxels in the following.

	600 vox. STDV 8		500 vox. STDV 8		600 vox. STDV 10		500 vox. STDV 10
Random seed configuration	1/10, 2/9, 28/57		1/10, 2/9, 28/57		1/10, 2/9, 28/57		1/10, 2/9, 28/57
Porosity	30%	60%	30%	60%	30%	60%	30%
Solid volume fraction SP1	35%	20%	35%	20%	35%	20%	35%
Solid volume fraction SP2	35%	20%	35%	20%	35%	20%	35%
Mean relative conductivity (M-factor) SP1	0.1176	0.0224	0.1175	0.0206	0.1208	0.0232	0.1226
Mean difference relative conductivity (M-factor) (SP1-SP2)/SP1	0.99%	4.84%	3.88%	9.41%	0.69%	5.11%	4.79%
Max difference relative conductivity (M-factor) (SP1-SP2)/SP1	1.59%	-7.74%	5.12%	10.76%	1.96%	-8.33%	7.15%
Mean volume specific interface area pore-SP2	1.711	1.853	1.711	1.852	1.729	1.870	1.730
Mean difference volume specific interface area pore-SP1/SP2 (SP1-SP2)/SP1	0.59%	0.46%	0.59%	0.43%	0.42%	0.34%	0.37%
Max difference volume specific interface area pore-SP1/SP2 (SP1-SP2)/SP1	0.82%	0.64%	0.82%	0.70%	0.63%	0.50%	0.57%
Mean volume specific contiguous TPB-length	12.696	6.970	12.701	6.901	12.820	7.008	12.823
STDV volume specific contiguous TPB-length	0.040	0.035	0.063	0.099	0.015	0.041	0.033

Fig. 10 Random seed study for the pluri-Gaussian structures. The reported values are averaged for three different random seed configurations.

To account for different statistical realizations a variation of the random seed is studied. The most important metrics are summarized in Fig. 10 for the mean values averaged for three different random seeds, for a characteristic structure size of 8 and 10 voxels standard deviations (STDV) for the PGMs and for a porosity of 30 % and 60 % and equal solid volume fractions of the solid phases. For a porosity of 30 %, the relative conductivities of the solid phases deviate about 1-2 % from each other for the structure sizes of 600^3 voxels. Therewith, the structure with the higher resolution of STDV = 10 voxels shows a similar self-consistency. Moreover, the conductivities are slightly higher for the higher resolution, probably because the bottlenecks are better resolved. For a structure size of 500^3 voxels, the deviation of the relative conductivities of the two solid phases is significantly higher, around 4 % for STDV 8 and around 5 % for STDV 10. For a porosity of 60 % and a solid volume fraction of 20 % for each of the solid phases, the uncertainty on a percentage basis

is generally significantly higher because of the lower absolute values. The deviations of the relative conductivities of the two solid phases for the 600^3 voxels structures is around 5 % and similar for both STDVs. For a structure size of 500^3 voxels, the deviations are around 10 %. The deviations of the volume specific interface areas of the two solid phases, which are theoretically equal as well, are in the range of 1 % and therewith sufficiently accurate for all the cases. The uncertainty of the TPB-length, estimated by the standard deviation of the three realizations, is uncritical as well. However, the deviations are significantly lower for a structure size of 600^3 voxels. To sum it up, the 600 voxels structure with an STDV = 10 voxels for the PGM seems to be the best choice.

E Reference dataset of a virtual PGM structure variation with neutral wetting

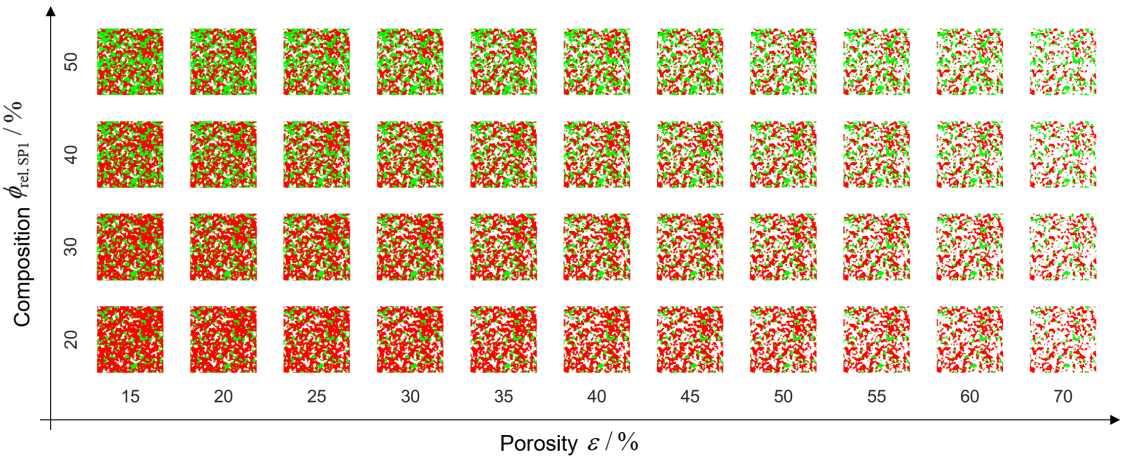

Fig. 11 Virtual microstructure variation for different porosities and compositions with PGM using neutral wetting (NW) conditions (i.e., $\alpha = 45°$ and $\beta = \gamma = 0°$). This PGM-NW dataset is symmetric with respect to the composition of SP1:SP2=50:50.

As a reference dataset, a virtual microstructure variation is performed with the PGM for different porosities and solid-phase compositions using neutral wetting conditions (i.e., using fixed threshold angles of $\alpha = 45°$ and $\beta = \gamma = 0°$) and without morphological manipulations (i.e., without step 4 of the workflow illustrated in Fig. 10 of the main article). The parameter variation is illustrated by the 2D orthoslices of the 3D structures, in in Fig. 11. This dataset represents typical features of well-sintered SOC microstructures in an idealized form. The identical wetting behaviour of the two solid phases results in a symmetric behaviour of many properties with respect to the composition. Thus, this study enables distinguishing between general microstructure effects (e.g., directly resulting from composition and porosity) and effects related to the wetting behaviour and morphological details (e.g., bottlenecks) of the solid phases. The abbreviation PGM-NW will be used to refer to this dataset. Note that because of the neutral wetting conditions, the two solid phases are interchangeable. Thus, for example the composition of SP1:SP2=80:20 can be deduced from the composition SP1:SP2=20:80 by simply exchanging SP1 with SP2. Those structures are not computed separately, but the data is mirrored to obtain the full compositional range, as shown in the plots. For an easier comparison with the more realistic structure variation reported in section 3.5 of the main article, the voxel size of the PGM-NW dataset is adapted to approximately fit the characteristic size of the phases and thus the volume specific interface areas.

In Figs. 12 - 14, a selection of microstructure properties is reported, which are typically used for the parametrization of a continuum multiphysics electrode model as e.g., discussed in chapters 9 and 10 of the PhD thesis by Ph. Marmet[4]. Even though this dataset represents general idealized microstructures, the results are presented specifically for the LSTN-CGO ceramic composite (i.e., SP1 = CGO and SP2 = LSTN).

Fig. 12 represents the contour plots for volume specific interface areas and TPB-length as a function of the total solid volume fraction ϕ_{tot} (i.e., 100% - porosity, respectively) and the relative volume fraction of

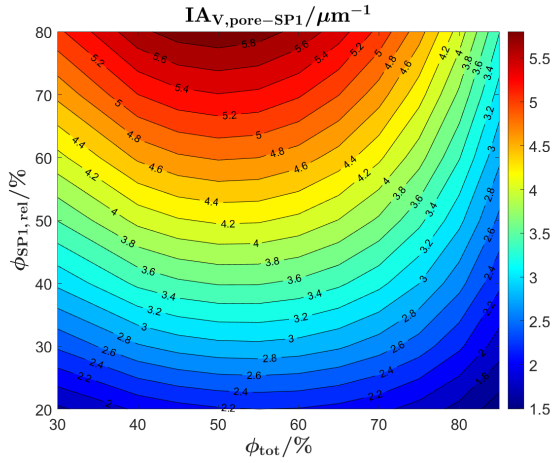

(a) Volume specific interface area pore-SP1 $IA_{V,pore-SP1}$

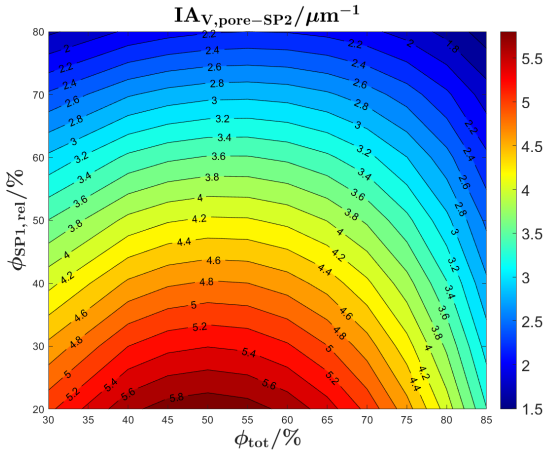

(b) Volume specific interface area pore-SP2 $IA_{V,pore-SP2}$

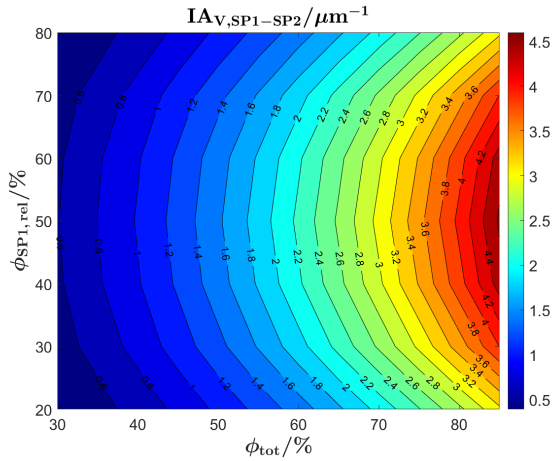

(c) Volume specific interface area SP1-SP2 $IA_{V,SP1-SP2}$

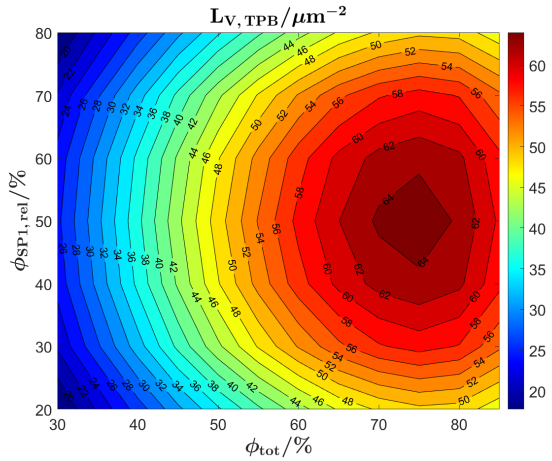

(d) Volume specific three-phase boundary length $L_{V,TPB}$

Fig. 12 PGM-NW dataset: contour plots of the volume specific interface areas (IA_V) a)-c) and the three-phase boundary length ($L_{V,TPB}$) d) as a function of the total solid volume fraction ϕ_{tot} (i.e., 100 % - porosity, respectively) and the relative volume fraction of SP1 $\phi_{SP1,rel}$ (i.e., composition, respectively).

SP1 $\phi_{SP1,rel}$ (i.e., composition, respectively). The volume specific pore-SP1 and pore-SP2 interface areas (Fig. 12 a) and b)) both represent potential reaction sites for MIEC electrodes (e.g., pore-CGO and pore-LSTN interfaces) and are thus important for the reaction kinetics. Because of the neutral wetting behaviour and the identical characteristic structure size of the two solid phases, the two properties are related to each other by a mirror-operation with respect to the $\phi_{SP1,rel} = 50\,\%$ line. Moreover, they show a maximum of the interface areas for a porosity of $\varepsilon = 50\,\%$ (i.e., $\phi_{tot} = 50\,\%$ respectively). The volume specific SP1-SP2 interface area (Fig. 12 c)) is a measure of the connection between the two solid phases. It is maximal for the highest total solid volume fraction (lowest porosity, respectively) and for a composition of 50:50 ($\phi_{SP1,rel} = 50\,\%$). The TPB-length (Fig. 12 d)) is an important parameter for the reaction kinetics as well, especially for the common Ni-YSZ electrodes. The maximal value is found at a composition of 50:50 and a total solid volume fraction of about $\phi_{tot} = 75\,\%$ (i.e., porosity of 25 %, respectively).

In Fig. 13 the relative conductivities are reported. The relative single-phase conductivity of SP1 (i.e., CGO) is obviously maximal for a large total solid volume fraction ϕ_{tot} (i.e., low porosity) and a high SP1-content $\phi_{SP1,rel}$ (see Fig. 13 c)). Correspondingly, the relative single-phase conductivity of SP2 (i.e., LSTN) is obviously maximal for a large total solid volume fraction ϕ_{tot} (i.e., low porosity) and a high SP2-content $\phi_{SP2,rel} = 100\,\% - \phi_{SP1,rel}$ (see Fig. 13 d)). Note that for this idealized dataset, $\sigma_{rel,SP2}$ can be obtained by mirroring of $\sigma_{rel,SP1}$ at the line $\phi_{SP1,rel} = 50\,\%$.

The relative single-phase conductivities are important for composites like Ni-YSZ, where the transport of

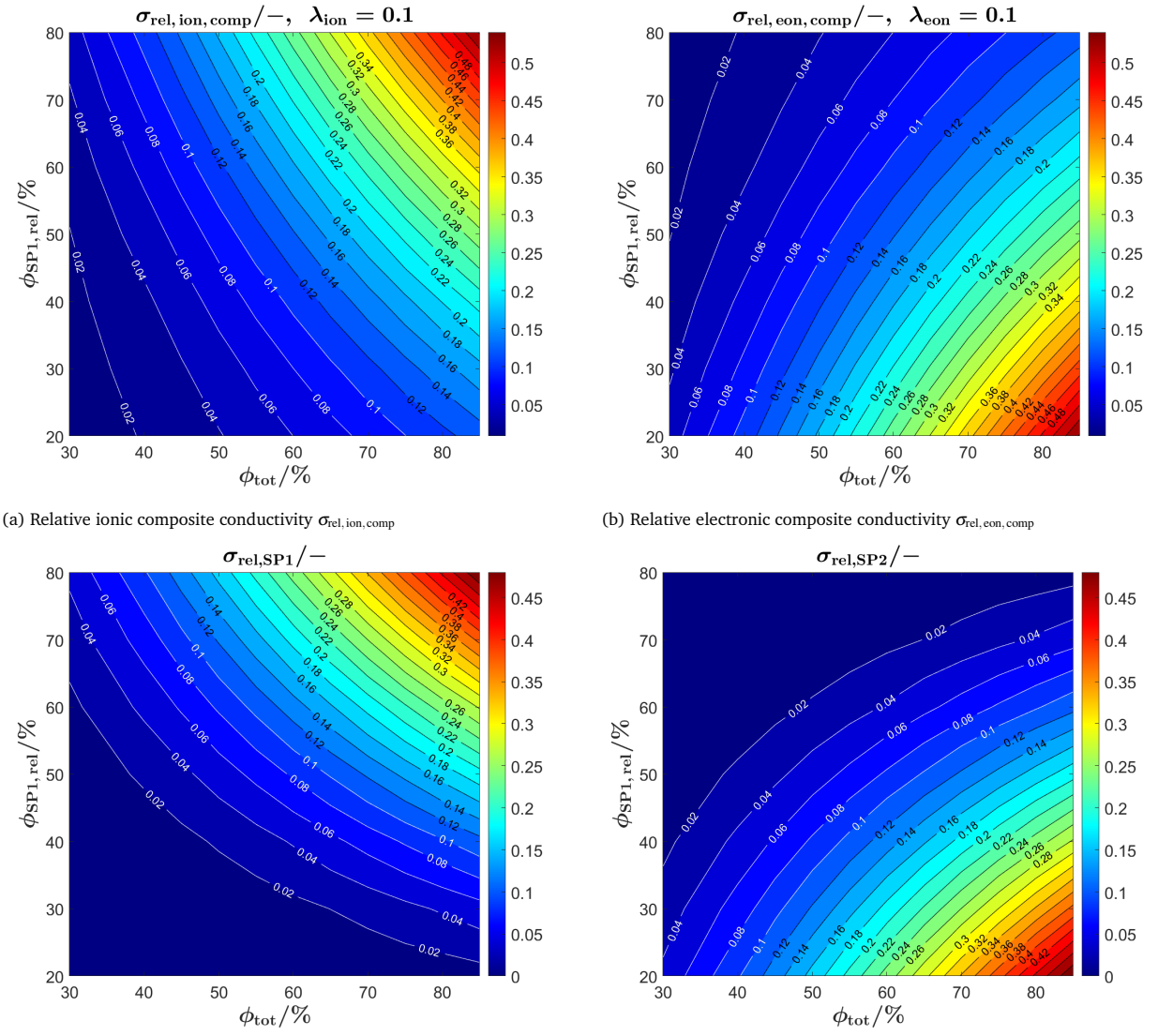

(a) Relative ionic composite conductivity $\sigma_{\mathrm{rel,ion,comp}}$

(b) Relative electronic composite conductivity $\sigma_{\mathrm{rel,eon,comp}}$

(c) Relative single-phase conductivity of the isolated SP1 (CGO-phase) $\sigma_{\mathrm{rel,SP1}}$

(d) Relative single-phase conductivity of the isolated SP2 (LSTN-phase) $\sigma_{\mathrm{rel,SP2}}$

Fig. 13 PGM-NW dataset: Contour plots of a) the relative ionic and b) the relative electronic composite conductivity and the (hypothetical) single-phase conductivities of c) the SP1 (CGO-phase) and d) the SP2 (LSTN-phase) as a function of the total solid volume fraction ϕ_{tot} (i.e., $100\,\%$ - porosity, respectively) and the relative volume fraction of SP1 $\phi_{\mathrm{SP1,rel}}$ (i.e., composition, respectively)). Note: the composite conductivities are computed for fixed ratios of intrinsic conductivities σ_0 in the two solid phases (i.e., ratio of the intrinsic ionic $\lambda_{\mathrm{ion}} = \frac{\sigma_{0,\mathrm{ion,LSTN}}}{\sigma_{0,\mathrm{ion,CGO}}}$ and electronic $\lambda_{\mathrm{eon}} = \frac{\sigma_{0,\mathrm{eon,CGO}}}{\sigma_{0,\mathrm{eon,LSTN}}}$ conductivities).

electrons and ions happens in separate phases. In this context, they describe the microstructure effect on the transport relating the intrinsic with the effective conductivities (i.e., $\sigma_{\mathrm{eff,SP1}} = \sigma_{\mathrm{rel,SP1}} \cdot \sigma_{0,\mathrm{SP1}}$). However, in the LSTN-CGO composite both phases are MIECs, which results in significantly higher effective composite conductivities compared to the single-phase conductivities, as the transport of electrons and ions are no more restricted to one solid phase. Hence, the composite conductivities are the relevant properties in this case, while the single-phase conductivities can only be used as hypothetical references.

In contrast to the single-phase conductivities, the microstructure effects for composite conductivity cannot be formulated independent from the intrinsic conductivities. Therefore, definitions for the relative ionic composite conductivities were introduced in a previous publication (Marmet et al.[2]) as a function of the ratio of intrinsic conductivities (i.e., ratio of the intrinsic electronic $\lambda_{\mathrm{eon}} = \frac{\sigma_{0,\mathrm{eon,SP1}}}{\sigma_{0,\mathrm{eon,SP2}}} \leq 1$ and ionic $\lambda_{\mathrm{ion}} = \frac{\sigma_{0,\mathrm{ion,SP2}}}{\sigma_{0,\mathrm{ion,SP1}}} \leq 1$ conductivities of the two solid phases). According to the estimations for the LSTN-CGO composite reported in table 4 of the main article, the intrinsic ionic conductivity of CGO is about a factor of 10 higher compared to

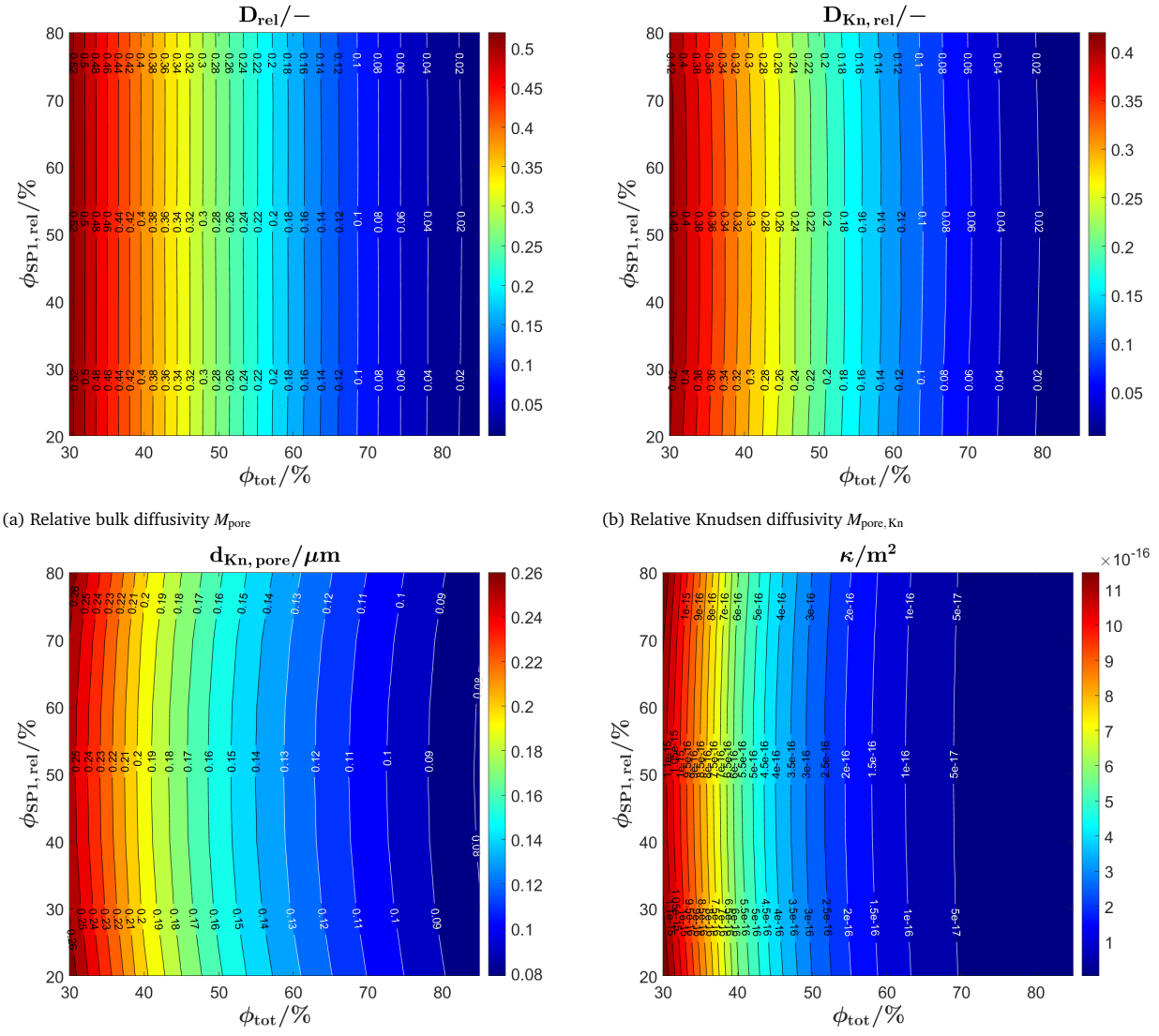

(a) Relative bulk diffusivity M_{pore}

(b) Relative Knudsen diffusivity $M_{\text{pore,Kn}}$

(c) Knudsen characteristic length $d_{\text{pore,Kn}}$

(d) Gas permeability κ

Fig. 14 PGM-NW dataset: Contour plots illustrating the effective transport properties of the pore-phase: a) bulk diffusivity, b) Knudsen diffusivity, c) Knudsen characteristic length and d) permeability as a function of the total solid volume fraction ϕ_{tot} (i.e., $100\,\%$ - porosity, respectively) and the relative volume fraction of SP1 $\phi_{\text{SP1,rel}}$ (i.e., composition, respectively).

LSTN, resulting in an intrinsic conductivity ratio of $\lambda_{\text{ion}} = 0.1$. In contrast, the intrinsic electronic conductivity of LSTN is about a factor of 10 higher compared to CGO, resulting in an intrinsic conductivity ratio of $\lambda_{\text{eon}} = 0.1$. The corresponding relative ionic and electronic composite conductivities are reported in Fig. 13 a) and b), respectively. The relative ionic composite conductivity has its maximum at the same corner as the single-phase conductivity of SP1 (CGO), as the influence of the LSTN-phase vanish for high CGO-contents. However, the reduction of the ionic composite conductivity with decreasing SP1-content (CGO) in a) is much less steep compared to the single-phase conductivity in c), because SP2 (LSTN) contributes as well to the composite conductivity (although it has a lower intrinsic conductivity). The enhancement of the relative composite conductivity compared to the single-phase conductivity is especially large for low volume fractions of SP1 (CGO), where bottlenecks and islands in SP1 can be bridged by SP2 (LSTN). This effect results in a much larger enhancement of the ionic composite conductivity with respect to the single-phase conductivity of SP1 than only the single-phase contribution of SP2 with its relatively low ionic conductivity. For the relative electronic composite conductivity (Fig. 13 b)), the same behaviour can be observed vice versa. Note that the relative electronic composite conductivity can be obtained by mirroring the relative ionic

composite conductivity the line $\phi_{\mathrm{SP1,rel}} = 50\,\%$, because of the neutral wetting behavior and the same intrinsic conductivity ratio $\lambda_{\mathrm{eon}} = \lambda_{\mathrm{ion}} = 0.1$. A detailed discussion of the composite conductivity and its implications on the microstructure design is beyond the scope of the present paper, but these issues will be discussed in great detail in a separate publication that is focusing specifically on composite conductivity.

The contour plots of the microstructure properties relevant for the gas transport according to the dusty gas model (see previous publications by Marmet et al.[2,5]) are plotted in Fig. 14. The relative diffusivities for bulk (Fig. 14 a)) and Knudsen (Fig. 14 b)) diffusion decrease with decreasing porosity (i.e., increasing total solid volume fraction ϕ_{tot}), while the values are almost constant with respect to the composition $\phi_{\mathrm{SP1,rel}}$. The Knudsen characteristic length (Fig. 14 c)) decreases with decreasing porosity. There is also a weak symmetric dependency on the composition. Slightly larger pores result if one solid phase has a dominant volume fraction. A similar behaviour is observed for the gas permeability (Fig. 14 d)), with the difference that the dependency on the porosity (and associated pore size) is more pronounced, which is a direct result of the quadratic relation of the permeability κ with the hydraulic radius r_{hc} (i.e., $\kappa \propto r_{\mathrm{hc}}^2$, see Marmet et al.[2]).

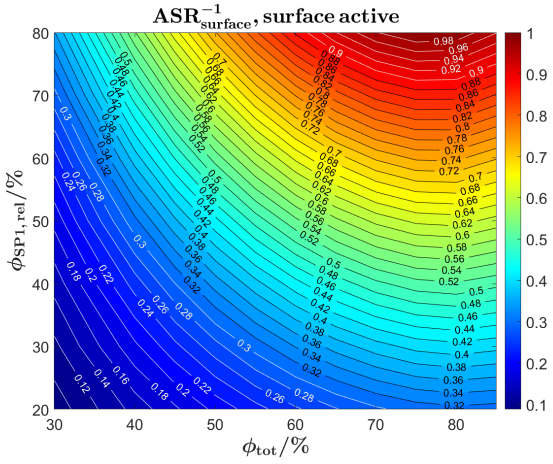

(a) Surface active electrode:
$ASR^{-1}_{\mathrm{surface}} \propto \sqrt{\sigma_{\mathrm{rel,ion,comp}} \cdot IA_{\mathrm{V,pore-CGO}}}$ (see Eq. 10 in the main article)

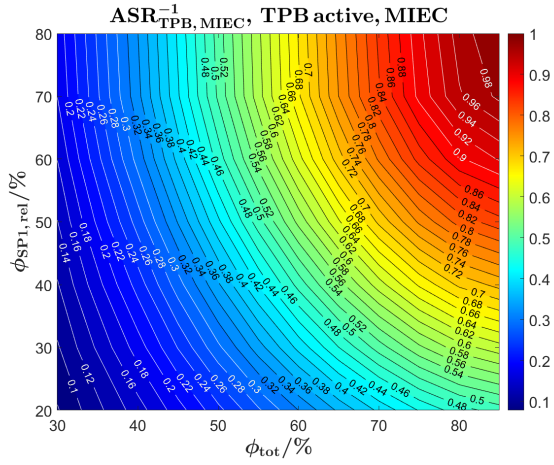

(b) TPB active MIEC electrode:
$ASR^{-1}_{\mathrm{TPB,MIEC}} \propto \sqrt{\sigma_{\mathrm{rel,ion,comp}} \cdot L_{\mathrm{V,TPB}}}$ (see Eq. 16)

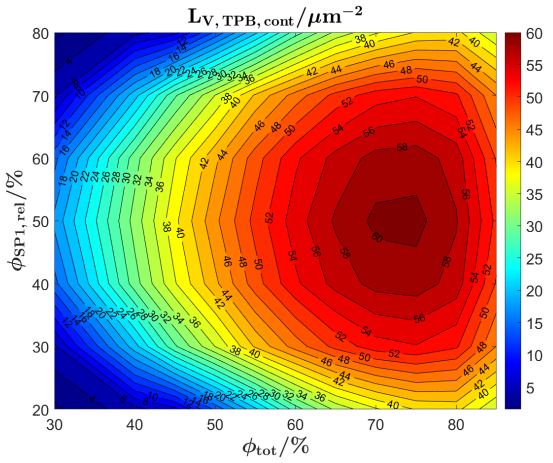

(c) Contiguous volume specific the three-phase boundary length $L_{\mathrm{V,TPB,cont}}$

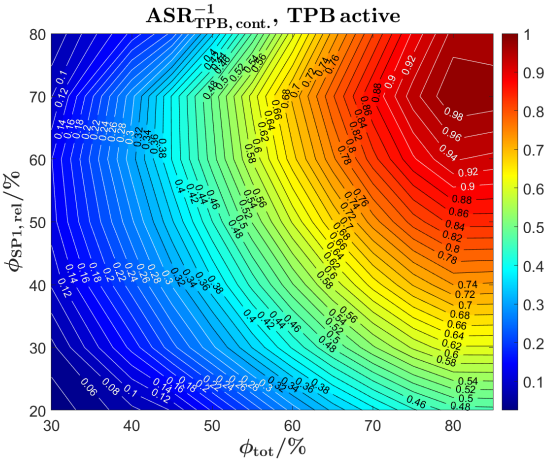

(d) Classical contiguous TPB active electrode (e.g., Ni-YSZ):
$ASR^{-1}_{\mathrm{TPB,cont.}} \propto \sqrt{\sigma_{\mathrm{rel,SP1}} \cdot L_{\mathrm{V,TPB,cont}}}$ (see Eq. 11 in the main article)

Fig. 15 Figures of merit for the performance of a) surface active electrodes, b) TPB active MIEC electrodes, d) classical TPB active electrodes (e.g., Ni-YSZ) and c) the corresponding contiguous three-phase boundary length ($L_{\mathrm{V,TPB,cont}}$) as a function of the total solid volume fraction ϕ_{tot} (i.e., $100\,\%$ - porosity, respectively) and the relative volume fraction of SP1 $\phi_{\mathrm{SP1,rel}}$ (i.e., composition, respectively).

As a first estimate of the electrode performances associated with the simulated microstructure variations, some figures of merit that can be estimated with a simplified approach were reported in section 3.5 of the main article according to the analytical model presented by Adler et al.[6]. As a reference, these figures of

merit are also reported for the PGM-NW dataset in Fig. 15. The principal behaviour is similar compared to the corresponding figures of merit of the DT-dataset (see Fig. 17 in section 3.5 of the main article and Fig. 27 in section G). The differences are discussed at the corresponding discussions of the DT-dataset, where this is useful.

F Detailed description of the digital twin construction

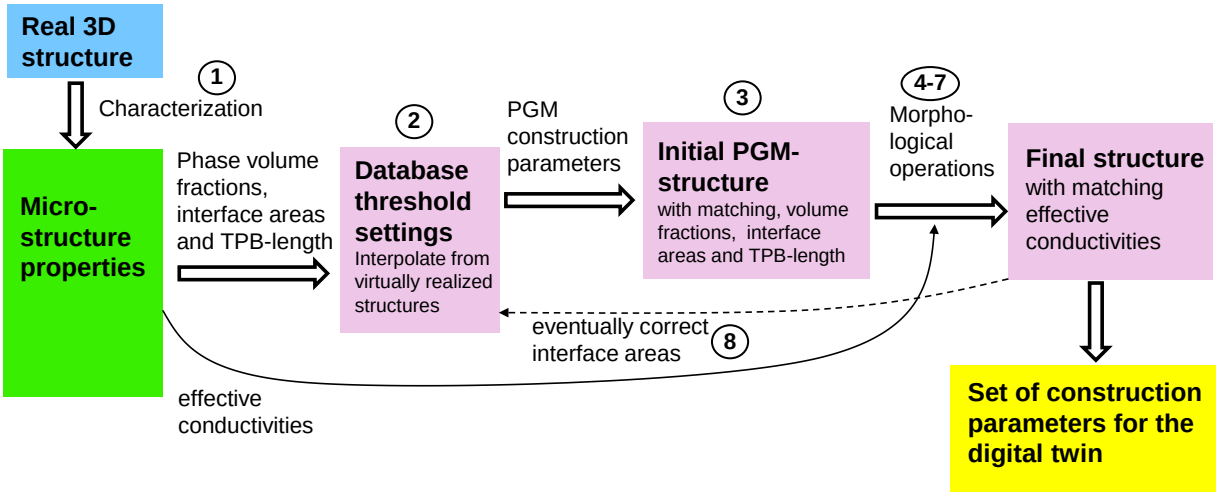

Fig. 16 Workflow for the construction of a stochastic digital microstructure twin.

In Fig. 16 a graphical overview of the digital twin construction workflow is presented and briefly described in the following. The individual steps are then reported in further detail and illustrated for the example of the CGO40-LSTN60 microstructure in the following subsections.

1. Standard characterization of the segmented real structure from 3D tomography using the characterization-app[2].

2. Interpolation of the structure database to determine appropriate threshold angles α, β and γ, which match the volume specific interface areas and TPB-length of the real structure with given phase volume fractions. Thereby, also the voxel size is scaled, while the number of voxels for the standard deviations of the Gaussian random fields are held constant at $SD_{\mathrm{GRF1}} = SD_{\mathrm{GRF2}} = 10\,\mathrm{voxels}$.

3. Generation of an initial PGM-structure with the correct porosity and composition using the interpolated threshold-angles.

4. Initial reduced characterization of the PGM-structure for single and composite conductivities, volume specific interface areas and TPB-length.

5. Optimization of the relative single-phase conductivity of the phase with lower volume fraction (minor phase) with morphological operations. The second involved phase for the morphological operations is the other solid-phase with the higher volume fraction (major phase) and the pore-phase remains unchanged.

6. Optimization of the relative single-phase conductivity of the major phase. The second involved phase for the morphological operations is the pore-phase and the already optimized minor phase remains unchanged.

7. If one or both solid-phase materials are MIECs, the relative composite conductivities are of major importance. For the resulting structure with the matched relative single-phase conductivities, the corresponding relative composite conductivities are determined as a next step. The morphological operations can

then be adapted to match the relative composite conductivities at the cost of a worse match of the single-phase conductivities.

8. If the conductivities are acceptable, the volume specific interface areas and TPB-length of the modified microstructure needs to be checked again, as the morphological operations do also change these properties. If necessary, the PGM-structure can be corrected in order that the interface areas and TPB-length match for the structure modified with the morphological operations.

For the morphological operations (step 5 and 6) it is favourable that first the minor solid-phase and subsequently the major solid-phase is optimized to match the relative conductivities. This is especially important for significantly different volume fractions of SP1 and SP2. If a set of digital twins shall be used for a parameter variation, this means that the order of the morphological operations for SP1 and SP2 needs to be changed near the composition of SP1:SP2=50:50, which is controlled by the parameter Switch 1 as reported in table 3 of the main article. In order to provide a consistent interpolation of the construction parameters, the digital twin with the composition closest to SP1:SP2=50:50 needs to be constructed in both versions. The parameters $n_{\mathrm{vox,mod,SP1}}$ and $n_{\mathrm{vox,mod,SP2}}$ are the number of voxels to be used for the morphological operations in order to match the relative conductivity of the phases and are determined iteratively. A positive value thereby corresponds to a reduction and a negative value to an enhancement of the relative conductivity of the phase.

F.1 Step 1: Characterization of the real structure

The standardized characterization of the three LSTN-CGO anode microstructures is reported in a previous publication[2].

F.2 Step 2: Best fit for PGM construction parameters

A large number of PGM-structures have been realized for different total solid volume fractions (or porosity, respectively), different composition of the solid phases and thresholding angles as visualized in Fig. 17. The following parameter configurations have been realized:

- Realized total volume fractions $\phi_{\mathrm{tot}} = [40\,\%, 50\,\%, 60\,\%, 70\,\%, 80\,\%]$.
- Realized compositions SP1:SP2 = [50:50, 60:40, 70:30, 80:20].
  Comment: These compositions are realized for all the total volume fractions listed above. Moreover, the solid phases SP1 and SP2 can be interchanged to e.g., get the composition SP1:SP2 = 30:70.
- Realized threshold angles for the compositions SP1:SP2= 50:50:
  $\alpha = [15^\circ, 35^\circ, 45^\circ]$
  $\beta = [-60^\circ, -40^\circ, -20^\circ, 0^\circ, 20^\circ]$
  $\gamma = [-20^\circ, 0^\circ, 20^\circ, 40^\circ, 60^\circ]$
  Comment: the values for $\alpha = [55^\circ, 75^\circ]$ can be obtained by mirroring the data.
- Realized threshold angles for the compositions SP1:SP2 = [60:40, 70:30, 80:20] :
  $\alpha = [15^\circ, 35^\circ, 45^\circ, 55^\circ, 75^\circ]$
  $\beta = [-40^\circ, -20^\circ, 0^\circ, 20^\circ]$
  $\gamma = [-20^\circ, 0^\circ, 20^\circ, 40^\circ]$

In numbers: There are 80 realized structures with different threshold angles (and thus different wetting behaviour) for each total volume fraction and composition. For the composition with SP1:SP2= 50:50, 75 structures are realized, which corresponds to 150 structures, if the mirrored data is used. Therewith, there are 315 realized structures for each total volume fraction listed. These are in total 1575 structures. By interchanging the two solid phases, the number of represented structures is doubled to 3150 structures.

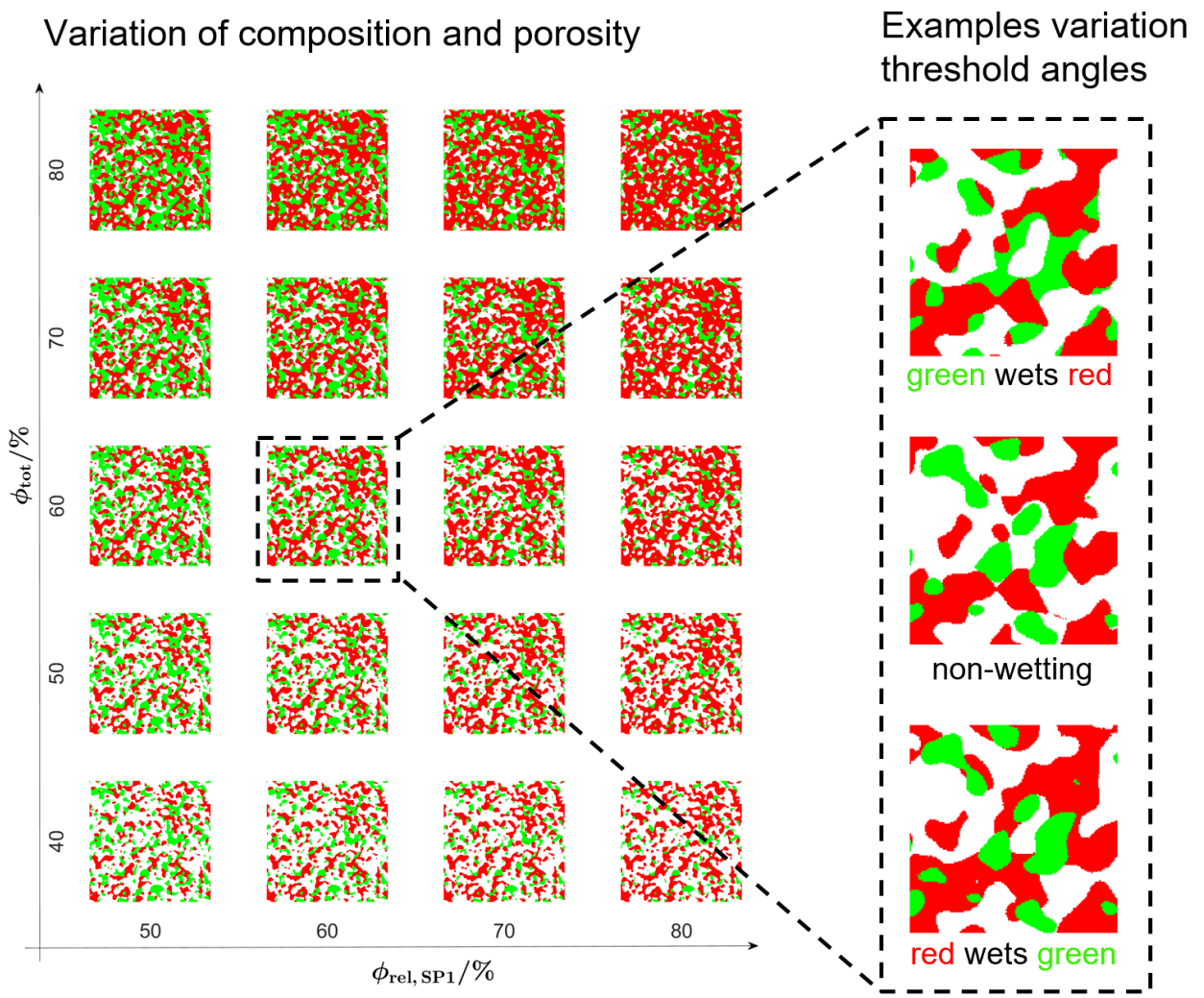

Fig. 17 Visualization of the PGM-structure library for the fitting of the construction parameters.

As an example, the volume specific interface areas for a $\phi_{\mathrm{tot}} = 60\,\%$ and a composition of 60:40 are plotted as a function of the threshold angle combinations in Fig. 18 a). Despite the quite large number of structures, the parameter sampling is still quite sparse. In order to get more points, the available data is interpolated and extrapolated using 3D interpolation algorithms available in Matlab[7]. The threshold angles are interpolated as follows:
$\alpha = [5° : 5° : 85°]$ (17 values)
$\beta = [-80° : 5° : 40°]$ (25 values)
$\gamma = [-40° : 5° : 80°]$ (25 values)
This results in 10625 threshold angle combinations. The interpolated interface areas for these threshold values are plotted in Fig. 18 b) again for the example of $\phi_{\mathrm{tot}} = 60\,\%$ and composition of 60:40. The first 1000 values are plotted separately in Fig. 18 c) to illustrate the details, which are no more resolved for the plot using the whole range.

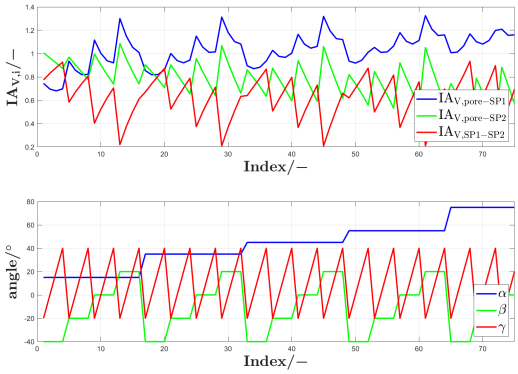

(a) Realized and characterized structures.

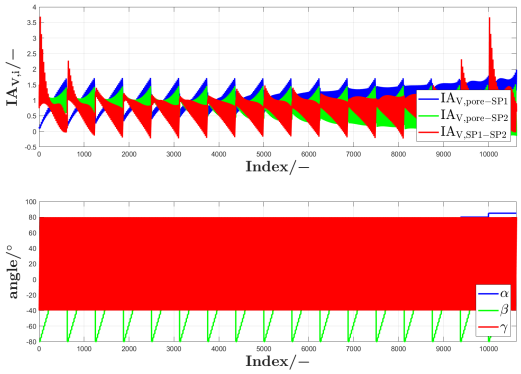

(b) Interpolated data for a large number of threshold angles.

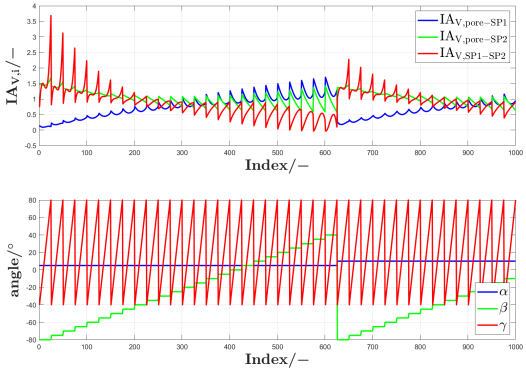

(c) Interpolated data for a large number of threshold angles, section of the first 1000 values.

Fig. 18 Threshold angle variation and corresponding volume specific interface areas for $\phi_{\text{tot}} = 60\,\%$ and a composition of 60:40: a) Realized structures, b) interpolated results, c) interpolated results for the section of the first 1000 values.

For the CGO40-LSTN60 structure used as an example, we first need to interpolate the available data to the present total volume fraction $\phi_{\text{tot}} = 49\,\%$ and a composition of CGO:LSTN=49:51. This is done by linear interpolation of the different datasets. The result of this interpolation are shown in Fig. 19 a), where the volume specific interface areas are plotted as a function of the threshold angle combinations. Therewith, we have an interpolated dataset of 10625 threshold angle combinations and associated interface areas for the actual total solid volume fraction and composition.

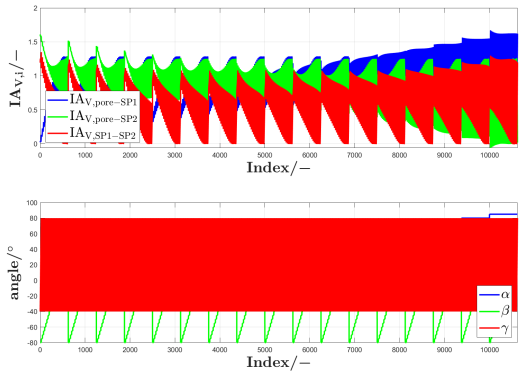

(a) Interpolated data for the actual case with $\phi_{tot} = 48.4\,\%$ and a composition of SP1:SP2=49:51.

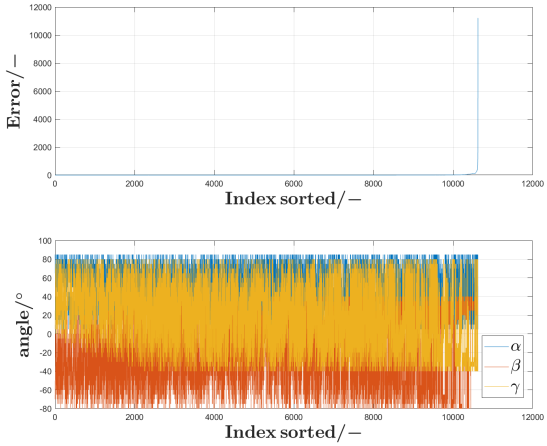

(b) Sorted error (smallest error first) for the available threshold-angle variations.

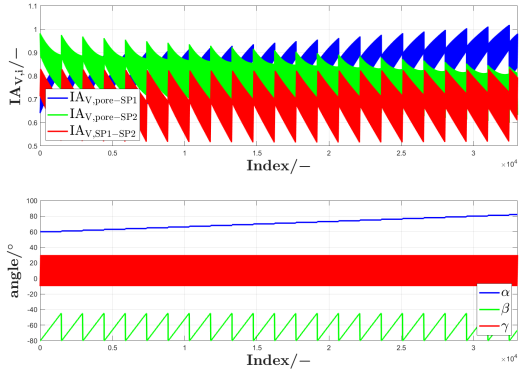

(c) Locally refined Interpolated data for the actual case with $\phi_{tot} = 48.4\,\%$ and a composition of SP1:SP2=49:51.

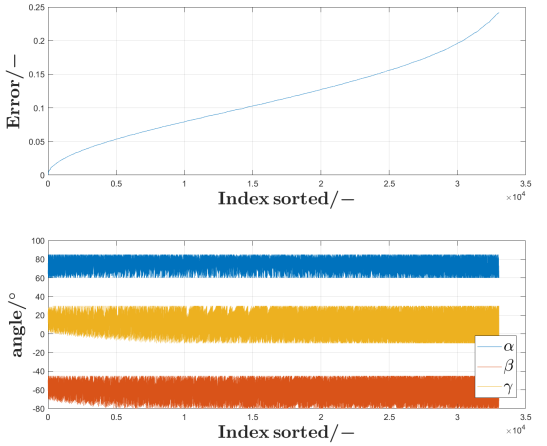

(d) Locally refined, sorted error (smallest error first) for the available threshold-angle variations.

Fig. 19 Interpolated data and error minimization for the CGO40-LSTN60 structure with $\phi_{tot} = 48.4\,\%$ and a composition of SP1:SP2=CGO:LSTN=49:51: a) interpolation for the full threshold angle range, b) error minimization for the full threshold angle range, c) interpolation for the locally refined threshold angle range around the optimum, d) error minimization for the locally refined threshold angle range.

We now want to choose the case which fits best to the real structure. Therefore, an error-criteria is specified, which then allows to chose the case with the smallest error. As the structure can be easily scaled, the relations between the volume specific interface areas are important and not the absolute values. Therefore, the interface areas normed to the volume specific interface area pore-SP1 are used:

$$IA_{\mathrm{V,pore-SP2,interp,norm}} = \frac{IA_{\mathrm{V,pore-SP2,interp}}}{IA_{\mathrm{V,pore-SP1,interp}}} \tag{2}$$

$$IA_{\mathrm{V,SP1-SP2,interp,norm}} = \frac{IA_{\mathrm{V,SP1-SP2,interp}}}{IA_{\mathrm{V,pore-SP1,interp}}} \tag{3}$$

Two error indicators are then formulated for the relation of the normed interface areas of the interpolated virtual structures and the reference values from the real structure:

$$\mathrm{Error}_{1,\mathrm{IA,pore-SP2}} = \frac{IA_{\mathrm{V,pore-SP2,interp,norm}}}{IA_{\mathrm{V,pore-SP2,norm,ref}}} \tag{4}$$

$$\mathrm{Error}_{1,\mathrm{IA},\mathrm{SP1-SP2}} = \frac{IA_{\mathrm{V},\mathrm{SP1-SP2},\mathrm{interp},\mathrm{norm}}}{IA_{\mathrm{V},\mathrm{SP1-SP2},\mathrm{norm},\mathrm{ref}}} \tag{5}$$

In order that the error has the same value for deviations in both directions (smaller and larger), the error indicators are modified with the following case discrimination:

$$\mathrm{Error}_{2,\mathrm{IA},\mathrm{pore-SP2}} = \begin{cases} \mathrm{Error}_{1,\mathrm{IA},\mathrm{pore-SP2}} & \text{for } \mathrm{Error}_{1,\mathrm{IA},\mathrm{pore-SP2}} \geq 1 \\ \left(\mathrm{Error}_{1,\mathrm{IA},\mathrm{pore-SP2}}\right)^{-1} & \text{for } \mathrm{Error}_{1,\mathrm{IA},\mathrm{pore-SP2}} < 1 \end{cases} \tag{6}$$

$$\mathrm{Error}_{2,\mathrm{IA},\mathrm{SP1-SP2}} = \begin{cases} \mathrm{Error}_{1,\mathrm{IA},\mathrm{SP1-SP2}} & \text{for } \mathrm{Error}_{1,\mathrm{IA},\mathrm{SP1-SP2}} \geq 1 \\ \left(\mathrm{Error}_{1,\mathrm{IA},\mathrm{SP1-SP2}}\right)^{-1} & \text{for } \mathrm{Error}_{1,\mathrm{IA},\mathrm{SP1-SP2}} < 1 \end{cases} \tag{7}$$

The error indicators are then added in the following way, which results in the following relation for the total error:

$$\mathrm{Error}_{\mathrm{tot},\mathrm{IA}} = \left|0.5 \cdot \mathrm{Error}_{2,\mathrm{IA},\mathrm{pore-SP2}} + 0.5 \cdot \mathrm{Error}_{2,\mathrm{IA},\mathrm{SP1-SP2}} - 1\right| \tag{8}$$

If the total error is zero, the match is perfect. The larger the error, the worse the cases fit to the real structure. For the current example, the sorted error is plotted (the smallest error is plotted first) for the different cases in Fig. 19 b). The corresponding threshold angles are plotted in the same figure bellow. This error was determined on interpolated data with 5° steps of the threshold angles. Therefore, the interpolation is refined in the region (±20° where possible) of the best case in 1° steps. The result of the refined interpolation is plotted in Fig. 19 c) and the error for the refined interpolation in Fig. 19 d). For this example, the minimal error is found for the threshold angles $\alpha = 35°$, $\beta = -27°$, $\gamma = 55°$ and a scaling factor of 0.2325 resulting in a voxel size of $l_{\mathrm{vox}} = 9.30\,\mathrm{nm}$

Optionally, the TPB-length can also be included directly into the optimization procedure. Therefore, an error indicator for the TPB-length is defined as follows:

$$\mathrm{Error}_{1,\mathrm{TPB}} = \frac{L_{\mathrm{TPB},\mathrm{interp}}}{\left(\frac{IA_{\mathrm{V},\mathrm{pore-SP1},\mathrm{interp}}}{IA_{\mathrm{V},\mathrm{pore-SP1},\mathrm{ref}}}\right)^2 L_{\mathrm{TPB},\mathrm{interp},\mathrm{ref}}} \tag{9}$$

where $\frac{IA_{\mathrm{V},\mathrm{pore-SP1},\mathrm{interp}}}{IA_{\mathrm{V},\mathrm{pore-SP1},\mathrm{ref}}}$ is the scaling factor between the interpolated virtual structure and the real reference structure, which has to be squared in order to account for the different scaling of the TPB compared to the interface areas. In order that the TPB-error has the same value for deviations in both directions (smaller and larger), the error indicator is modified with the following case discrimination:

$$\mathrm{Error}_{2,\mathrm{TPB}} = \begin{cases} \mathrm{Error}_{1,\mathrm{TPB}} & \text{for } \mathrm{Error}_{1,\mathrm{TPB}} \geq 1 \\ \left(\mathrm{Error}_{1,\mathrm{TPB}}\right)^{-1} & \text{for } \mathrm{Error}_{1,\mathrm{TPB}} < 1 \end{cases} \tag{10}$$

The expression for the total error including the TPB-length is then formulated as follows:

$$\mathrm{Error}_{\mathrm{tot},\mathrm{IA},\mathrm{TPB}} = \left|\mathrm{Error}_{2,\mathrm{IA},\mathrm{pore-SP2}} + \mathrm{Error}_{2,\mathrm{IA},\mathrm{SP1-SP2}} + W_{\mathrm{TPB}} \cdot \mathrm{Error}_{2,\mathrm{TPB}} - 2 - W_{\mathrm{TPB}}\right| \tag{11}$$

where W_{TPB} is a weighting-factor for the importance of the TPB-length (for $W_{\mathrm{TPB}} = 1$ the TPB-length has the same weight as the interface areas, for $W_{\mathrm{TPB}} = 0$ the TPB-length is not considered at all). This weighting-factor allows to define the importance of the properties. For example, for a Ni-YSZ electrode the TPB-length is very important, while for MIEC anodes the interface areas are more relevant.

F.3 Step 3: Generate initial PGM-structure

An initial PGM-structure with the correct porosity and composition and with the predicted best threshold angles to match the interface areas is generated. Also the scale is adapted to best fit the interface areas. An orthoslice of this structure is reported in Fig. 21. Details about the PGM-structure generation are documented in section 2.2 of the main article.

F.4 Step 4: Reduced characterization of the PGM-structure

A reduced characterization is performed for the resulting PGM-structure including single-phase and composite conductivities, volume specific interface areas and TPB-length. In Fig. 25, the microstructure properties of the pure PGM digital microstructure twin are compared to the tomography microstructure properties. The phase volume fractions, the interface areas and the TPB-length match very well. However, the relative composite and single-phase conductivities show quite large deviations. Therefore, the conductivities will be optimized with morphological operations in the next step. Note that for studies, for which such deviations for the relative conductivities are acceptable, the construction process can be finished at this step, using the pure PGM-structures.

F.5 Step 5: Optimize the relative conductivity of the phase with lower volume fraction with morphological operations

To improve the match of the relative conductivities, the solid phases can be modified with morphological operations. As a first step, the solid-phase with the lower volume fraction (minor phase) is modified. In our example case, this is SP1. In this case, SP2 is the counter phase. Starting from the pure PGM-structure (Fig. 20 a)), a dilate operation is performed on SP2, adding a certain amount of voxels at the surface of SP2. The phase SP1 is therewith reduced, while the pore-phase is held constant, as shown in Fig. 20 b). The process is then reversed and a dilate operation is performed on SP1, whereby voxels are added on the surface of SP1 until the ϕ_{SP1} is too high, as shown in Fig. 20 c). For the resulting structure, SP1 is now less connected and has more pronounced bottlenecks, while SP2 is now more connected and has less pronounced bottlenecks. The pore-phase remains again unchanged. To match the initial solid volume fractions more precisely, a dilate operation on SP2 is added with one voxel. The effect of this operation is then isolated by subtracting the structure of the last step as shown in Fig. 20 d). The solid volume fraction of this correction structure is computed and compared to the mismatch of ϕ_{SP1}. A GrainGeo template is then constructed (Fig. 20 e)) with the volume fraction corresponding to fraction of the correction structure needed to get the correct value for ϕ_{SP1}. This template is then applied on the correction structure, resulting in a new correction structure shown in Fig. 20 f), which is then added to SP1 to get again very close to the initial ϕ_{SP1}.

The relative single-phase conductivity of SP1 is now calculated for the modified structure. If the relative conductivity is still too high compared to the real structure, the process is automatically restarted with a larger number of voxels involved in the dilate operations. This process is repeated until the conductivity of the real structure is underestimated or until a maximum number of voxels for the dilate operations is reached. Typically, 6-7 voxels result in a still acceptable distortion of the structure. For larger values, the structure becomes awkward and the interface areas and three-phase boundary length do change strongly. Moreover, a single dilate step with several voxels result in rounder shapes than several dilate steps with only one voxel. Therefore, almost the whole dilate operation is done in one step and the single voxel steps are only used for fine-tuning. As an additional measure, isolated parts of the solid-phase to be modified (i.e., SP1 in our example), but which are connected to the other solid-phase (islands), are excluded from the morphological operations. Therewith, the total removement of small but realistic structure parts due to the morphological operations can be prevented. The manipulated structure after this step with morphological operations for SP1 is shown in Fig. 21 c).

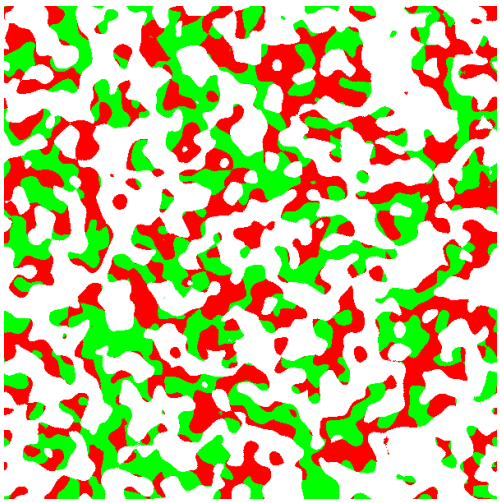

(a) Pure PGM digital twin structure, correction after morphological operations.

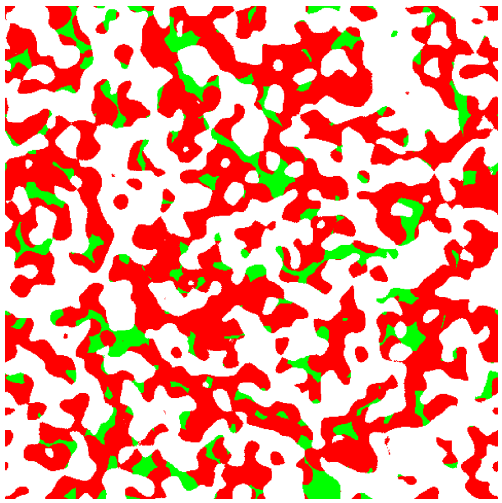

(b) Dilatation of SP2 (red) with SP2 and fixed pore-phase. SP1 (green) is thereby reduced.

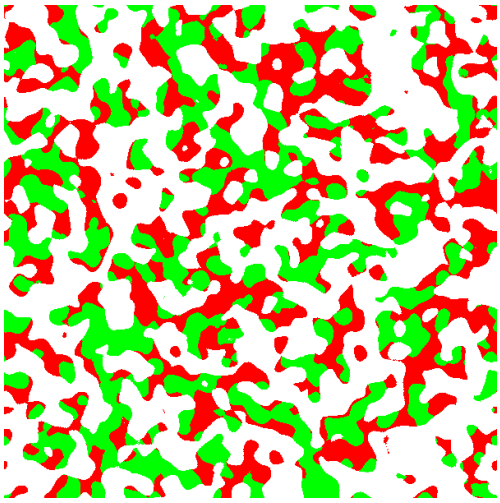

(c) Dilatation of SP1 (green) with SP1 and fixed pore-phase, raw version with too high ϕ_{SP1}.

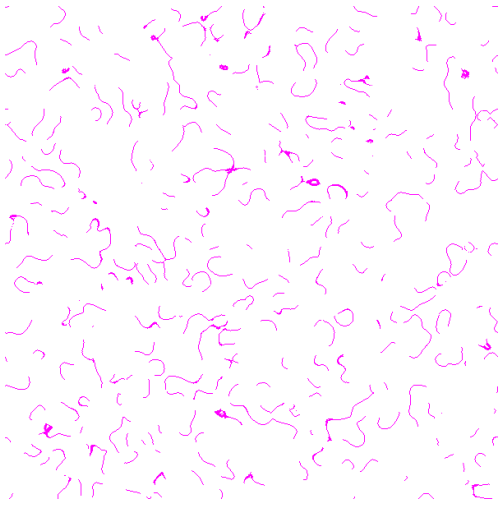

(d) Isolation of one SP2-SP2 dilatation step.

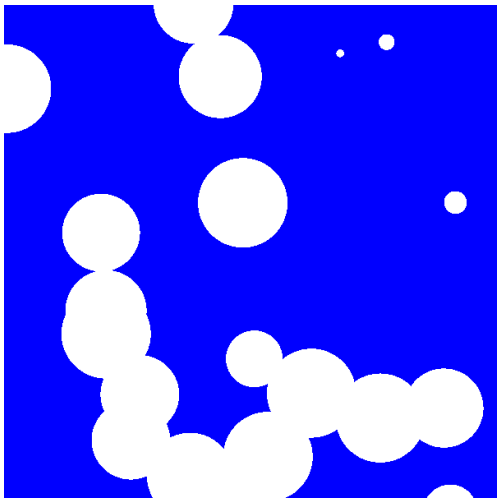

(e) GrainGeo stamp to correct the volume fractions.

(f) Structure to add to SP2 to correct the solid volume fractions, (stamp e) has been applied on d)).

Fig. 20 Morphological operations to optimize the conductivity of SP1. The central slices in the XZ-plane are shown for the 3D structures of the different steps.

F.6 Step 6: Optimize the relative conductivity of the phase with higher volume fraction with morphological operations

As a further step, the solid-phase with the higher volume fraction (major phase) is modified in the same manner as in step 5. In our example case, this is SP2. Thereby, the structure resulting from step 5 (Fig. 21 c)) is further modified. In this step, the counter-phase is now the pore-phase, while SP1 remains unchanged. Therewith, the relative single-phase conductivity of SP2 is decreased by simultaneously increasing the diffusivity of the pore-phase. For a case, where the relative single-phase conductivity of SP2 shall be increased and the diffusivity of the pore-phase shall be decreased, the two phases can simply be exchanged. The finished structure with morphological operations for SP1 and SP2 is shown in Fig. 21 d).

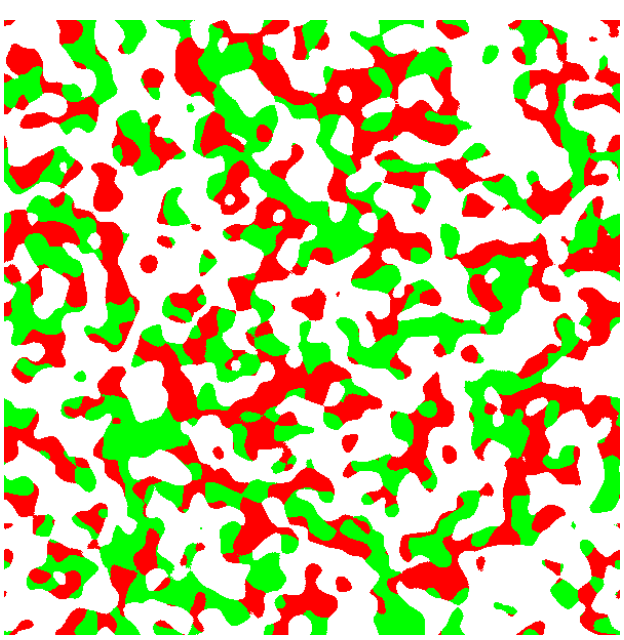

(a) Pure PGM digital twin structure, initial version.

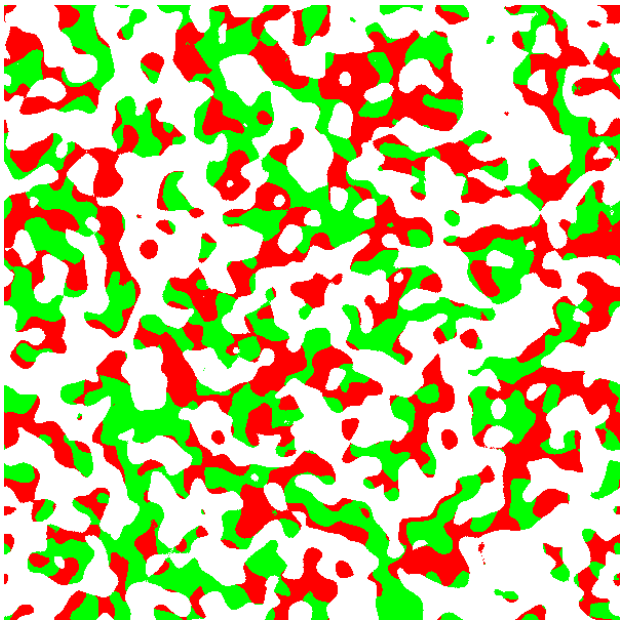

(b) Pure PGM digital twin structure, correction after morphological operations.

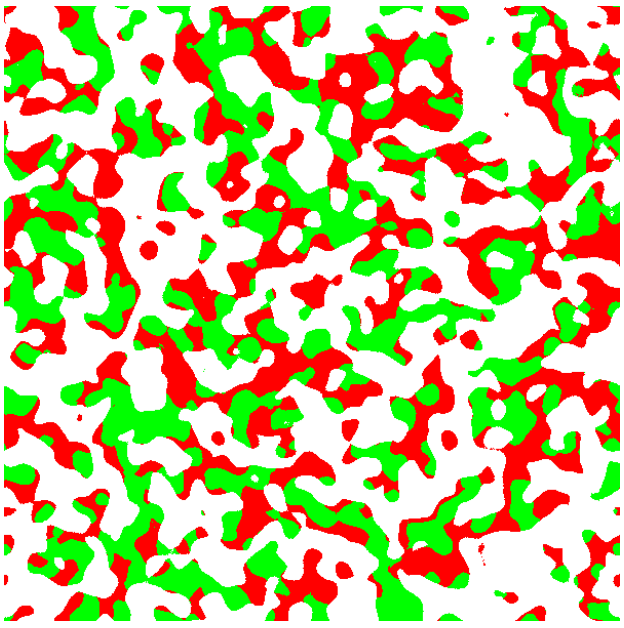

(c) PGM structure with manipulated SP1 (green) to match the composite conductivity.

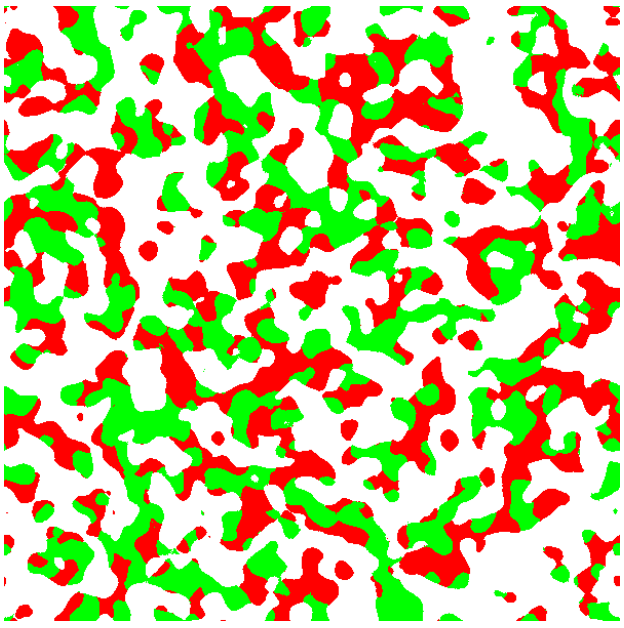

(d) Finished digital twin with manipulated SP1 (green) and SP2 (red) to match the composite conductivity.

Fig. 21 Morphological operations to optimize the composite conductivities, central slice in the XZ-plane. Colour code: green = CGO (SP1), red = LSTN (SP2), white = pore.

F.7 Step 7: Optimization of the relative composite conductivities

If one or both solid phase materials are MIECs, the relative composite conductivities are of major importance. For this case, this additional step 7 is needed to check and correct the composite conductivities. For the resulting structure with the matched relative single-phase conductivities the corresponding relative composite conductivities are determined as a next step. The morphological operations can then be adapted to match the relative composite conductivities. This can be done automatically, providing an initial guess for the number of voxels to involve for the dilate operation of both solid phases. The algorithm then adapts always the phase with the higher impact on the corresponding composite conductivity. As this algorithm does not provide perfect results yet, there is a second option to provide a list of voxel values for the dilate operation. The corresponding composite conductivities are then computed and the results can be judged manually. Note that the improvement of the relative composite conductivities comes at the cost of a worse match of the relative single-phase conductivities. However, for MIECs the relative composite conductivities are more important and therewith this drawback is bearable.

F.8 Step 8: Improvement of the interface areas by correcting the PGM-structure

Unfortunately, the morphological operations to match the composite conductivities distort the volume specific interface areas and the TPB-length as reported in Fig. 25, where the values for the pure PGM-structure and the structure after the composite conductivity optimization are compared. Especially the volume specific interface area SP1-SP2 is considerably reduced. The volume specific interface area pore-SP1 is slightly increased and the volume specific interface area pore-SP2 is slightly reduced by the morphological operations. This distortion can be limited by using a small number of voxels for the dilate operations, which is a trade-off with the good match of the relative conductivities. However, if the distortion is not too high, it can be corrected by changing the initial PGM-structure. Therefore, the target values of the volume specific interface areas are tuned to get an adapted PGM-structure, which compensates the distortion of the morphological operations. The target values are corrected as follows:

$$IA_{\mathrm{V,pore-SP1,ref,corr}} = \frac{IA_{\mathrm{V,pore-SP1,ref}}}{\left(\frac{IA_{\mathrm{V,pore-SP1,realized}}}{IA_{\mathrm{V,pore-SP1,ref}}}\right)^{1.5}} \tag{12}$$

$$IA_{\mathrm{V,pore-SP2,ref,corr}} = \frac{IA_{\mathrm{V,pore-SP2,ref}}}{\left(\frac{IA_{\mathrm{V,pore-SP2,realized}}}{IA_{\mathrm{V,pore-SP2,ref}}}\right)^{1.5}} \tag{13}$$

$$IA_{\mathrm{V,SP1-SP2,ref,corr}} = \frac{IA_{\mathrm{V,SP1-SP2,ref}}}{\left(\frac{IA_{\mathrm{V,pore-SP2,realized}}}{IA_{\mathrm{V,SP1-SP2,ref}}}\right)^{1.5}} \tag{14}$$

Note that the exponent of 1.5 is best practice and accounts for the fact that the deviation needs to be over-compensated to match the volume specific interface areas after the morphological operations. The optimized pure PGM-structure is reported in Fig. 21 b). The interface areas of the optimized pure PGM-structure are reported in Fig. 25 as well. Especially the volume specific interface area SP1-SP2 is significantly larger in order to compensate its reduction due to the morphological operations. Note that there is no need to repeat the optimization of the relative conductivities using the corrected PGM-structure. Normally it is sufficient to use the values determined by the first optimization. The deviations for the conductivities between the initial and the optimized PGM-structure for the same morphological operations are typically small as reported for our example in Fig. 25.

All the parameters for the PGM construction and the morphological operations can then be summarized to a construction plan for the digital twin structure as shown in Fig. 22. This parameter set allows for a fully automated generation of the stochastic digital twin microstructure and corresponding parameter variations.

Construction of the GRF

Description	Variable	Unit	Value
Name of the structure-file	StructureName	-	GRF_a12_bm27_g79_test.gdt
Number of voxels in X-direction	NX	vox	600
Number of voxels in Y-direction	NY	vox	600
Number of voxels in Z-direction	NZ	vox	600
Voxel length	VoxelLength	nm	9.16
Standard deviation of the Gaussfield of solid phase 1	StandardDeviation_SP1	vox	10
Standard deviation of the Gaussfield of solid phase 2	StandardDeviation_SP2	vox	10
Random seed for the GRF of solid phase 1	RandomSeed_GRF1	-	1
Random seed for the GRF of solid phase 2	RandomSeed_GRF2	-	10
Predefined solid volume fraction of solid phase 1	SVF_SP1_def	%	23.5471237
Predefined solid volume fraction of solid phase 2	SVF_SP2_def	%	24.8190059
Tolerance for the solid volume fractions	SVF_Tolerance	%	0.005
Angle between the threshold areas of solid phase 1 and 2	alpha	°	12
Angle between the threshold areas of solid phase 2 and pore phase	beta	°	-27
Angle between the threshold areas of solid phase 1 and pore phase	gamma	°	79
Dilation radius phase 0-1	DilationRadius_0_1	vox	0
Dilation radius phase 0-2	DilationRadius_0_2	vox	0
Dilation radius phase 1-2	DilationRadius_1_2	vox	0

Morphological operations

Description	Variable	Unit	Value
Step 1			Modify SP1 vs SP2
Number of voxels for the modification of step 1	n_vox_mod_step1	vox	6
Dilatation settings	Dilatation_settings	-	auto
Step 2			Modify SP2 vs pore-phase
Number of voxels for the modification of step 2	n_vox_mod_step2	vox	5

Fig. 22 Construction parameters of the digital microstructure twin.

F.9 Details digital microstructure twin for CGO40-LSTN60 sample

In this section the real tomography structure is compared with its digital microstructure twin and the deviations are discussed. Fig. 23 provides a visual comparison of two orthoslices of the real and virtual structure with the same scale. It has to be emphasized that it is not expected that the individual features are equal, but that the morphology of the real and corresponding virtual microstructure follow the same (or at least very similar) statistics. There is generally a very good visual agreement of the real and the virtual structure. However, also some differences are visible. In the real structure, there are some larger bulges of the CGO-phase (green) present, which is not captured by the homogeneous virtual structure. Moreover, the two solid phases are a bit more intermixed in the real structure.

In Fig. 25, a selection of microstructure properties is compared for the real and the virtual microstructures. The phase volume fractions match almost perfectly. The volume specific interface areas pore-SP1 and pore-SP2 also match very well with deviations in the sub-percentage range. The volume specific interface area SP1-SP2 and the TPB-length show a somewhat larger deviation around 2 %. The transport properties generally show larger deviations for the current example. The relative single-phase conductivities show the largest deviations around 40 %. However, they are not really relevant for the current case and the relative composite conductivities are optimized instead. The relative electronic composite conductivity matches quite well (deviation of 4 %) while the relative ionic composite conductivity shows a larger deviation of approximately 20 %. However, relative conductivities for phases with low volume fractions are generally hard to be predicted accurately, because of their dependency on small geometrical details. The pore-phase is generally expected to show larger deviations between real structure and digital microstructure twin, because the solid phases are optimized and the pore-phase is simply what is left over. However, for the current case with a quite large porosity of about 52 %, the prediction is quite robust. The relative (bulk) gas diffusivity is matched quite well (deviation of 10 %) and also the permeability is matched very well (deviation of 4 %). Also the parameters for the Knudsen diffusion (relative Knudsen diffusivity and Knudsen characteristic length) match surprisingly well with deviations less than 2 %. Note that the Knudsen diffusion is the dominant restriction for the gas diffusion in the current case.

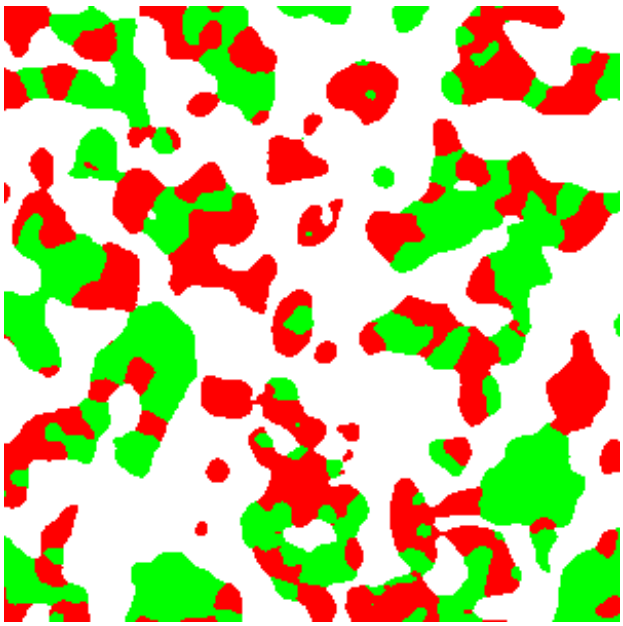

(a) Tomography, central slice in the XZ-plane.

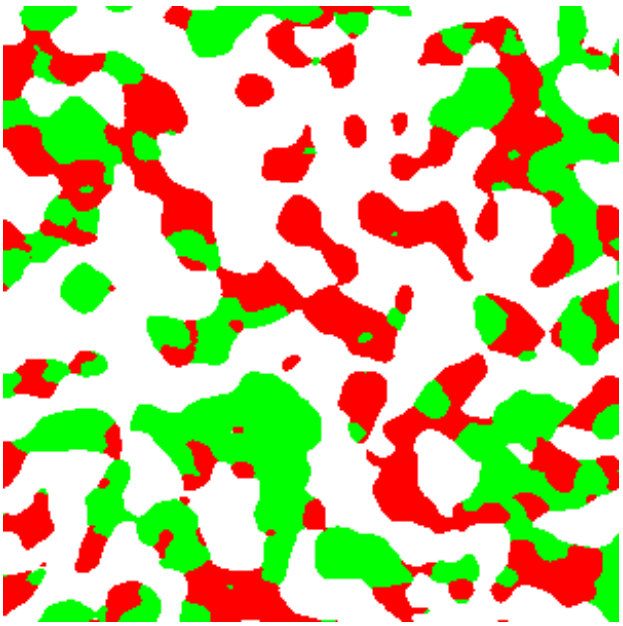

(b) Tomography, central slice in the YZ-plane.

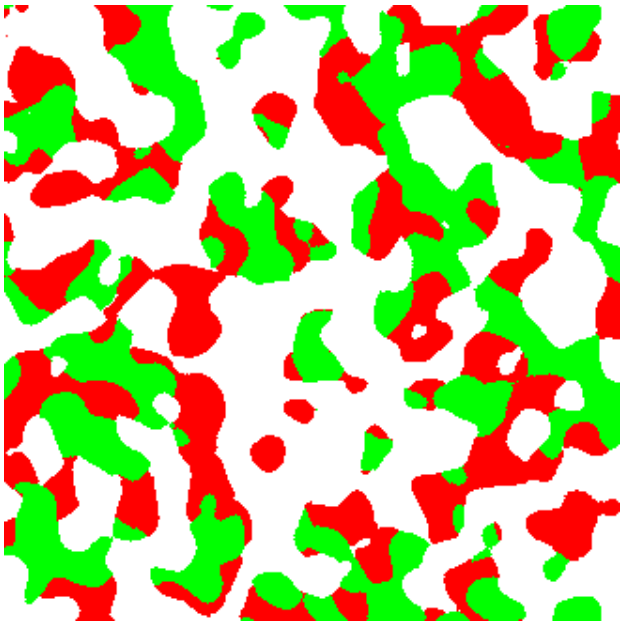

(c) Digital microstructure twin, central slice in the XZ-plane.

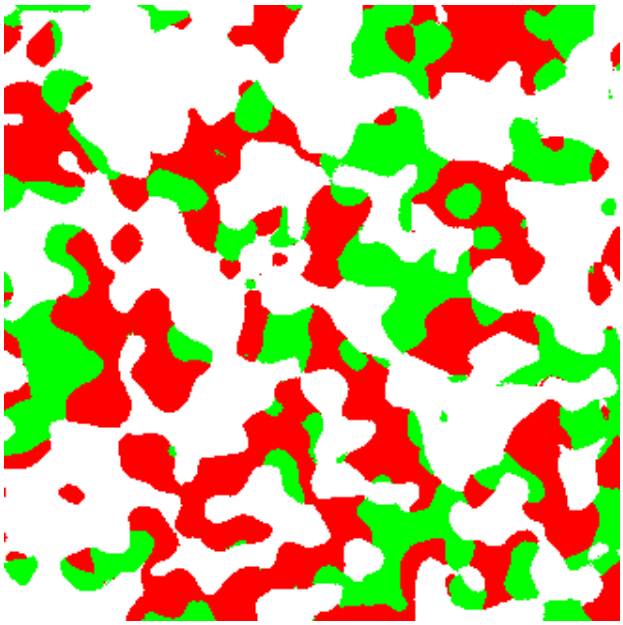

(d) Digital microstructure twin, central slice in the YZ-plane.

Fig. 23 CGO40-LSTN60 sample: comparison of orthoslices from tomography a),b) and digital microstructure twin reconstruction c),d). Colour code: green = CGO (SP1), red = LSTN (SP2), white/transparent = pore. The dimensions of the orthoslices are $3\,\mu m$ x $3\,\mu m$

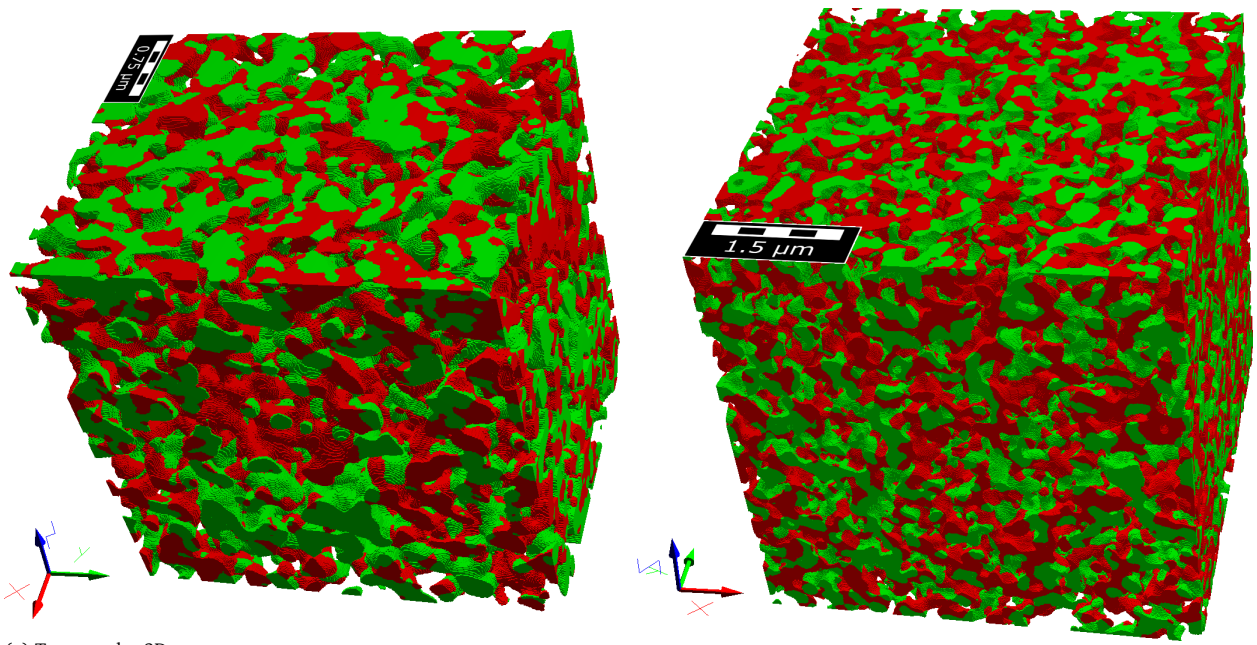

(a) Tomography, 3D structure.
Dimensions: 3 µm x 3.84 µm x 3.84 µm

(b) Digital microstructure twin, 3D structure.
Dimensions: 5.5 µm x 5.5 µm x 5.5 µm

Fig. 24 CGO40-LSTN60 sample: comparison of the 3D structures from tomography a) and digital microstructure twin reconstruction b) (with different scales). Colour code: green = CGO (SP1), red = LSTN (SP2), transparent = pore.

Case			Tomograpy	Digital Twin	Pure GRF	Comp. Cond. Mod	Pure GRF opt
Description	**Variable**	**Unit**	**Value**	**Value**	**Value**	**Value**	**Value**
Material for solid phase 1	Material_SP1	-	CGO	CGO	CGO	CGO	CGO
Material for solid phase 2	Material_SP2	-	LSTN	LSTN	LSTN	LSTN	LSTN
Voxel length	VoxelLength	nm	10	9.16	9.16	9.16	9.16
Number of voxels in X-direction	NX	vox	300	600	600	600	600
Number of voxels in Y-direction	NY	vox	384	600	600	600	600
Number of voxels in Z-direction	NZ	vox	384	600	600	600	600
Total porosity (volume fraction of the pore phase)	Epsilon	-	0.5163	0.5163	0.5163	0.5162	0.5164
Total solid volume fraction	SVF_tot	-	0.4837	0.4837	0.4837	0.4838	0.4836
Solid volume fraction SP1	SVF_SP1	-	0.2355	0.2352	0.2355	0.2353	0.2355
Solid volume fraction SP2	SVF_SP2	-	0.2482	0.2485	0.2482	0.2485	0.2482
Volume specific interface area pore phase - solid phase 1	IA_V_pore-SP1	mu^2/mu^3	3.295	3.295	3.284	3.350	3.168
Volume specific interface area pore phase - solid phase 2	IA_V_pore-SP2	mu^2/mu^3	3.813	3.819	3.818	3.711	3.936
Volume specific surface area of pores	S_V_pore	mu^2/mu^3	7.108	7.114	7.102	7.062	7.104
Volume specific interface area solid phase 1 - solid phase 2	IA_V_SP1-SP2	mu^2/mu^3	2.966	2.902	2.963	2.612	3.538
Volume specific three-phase boundary (TPB) length	L_TPB_V	mu/mu^3	67.894	69.591	65.268	62.523	72.531
Relative single-phase conductivity SP1	sigma_eff_Case1	S/m	0.0204	0.0291	0.0441		
Relative single-phase conductivity SP2	sigma_eff_Case2	S/m	0.0345	0.0473	0.0550		
Relative electronic composite conductivity λ_{eon} = 0.1	sigma_eff_Case4	S/m	0.0848	0.0880	0.0978	0.0874	
Relative ionic composite conductivity λ_{ion} = 0.1	sigma_eff_Case5	S/m	0.0689	0.0823	0.0885	0.0831	
Relative gas diffusivity simulated	D_rel_sim	-	0.3249	0.2930	0.2884		
Gas permeability simulated	Kappa_sim	m^2	4.382E-16	4.225E-16			
Knudsen characteristic length/ pore-diameter	KnudsenCharacteristicLength	um	0.1868	0.1889			
Knudsen relative diffusivity simulated X-direction	D_Kn_rel_sim_X	-	0.2071	0.2130			
Knudsen relative diffusivity simulated Y-direction	D_Kn_rel_sim_Y	-	0.2273	0.2208			
Knudsen relative diffusivity simulated Z-direction	D_Kn_rel_sim_Z	-	0.2351	0.2236			
Knudsen relative diffusivity simulated mean	D_Kn_rel_sim_XYZ_mean	-	0.2232	0.2192			

Fig. 25 Comparison of the microstructure properties of the tomography structure and the digital microstructure twin for the CGO40-LSTN60 sample.

The covariance functions of the real and virtual microstructure fit very well, despite the fact that they are not directly fitted. However, this good match is not surprising, as the covariance function reflects morphological properties of the microstructure, e.g., the slope of the covariance function at the y-axis intercept is directly related to the phase specific surface area (see e.g., Marmet et al.[2]), which is indeed directly fitted. This confirms that the chosen approach is well suited for this specific data.

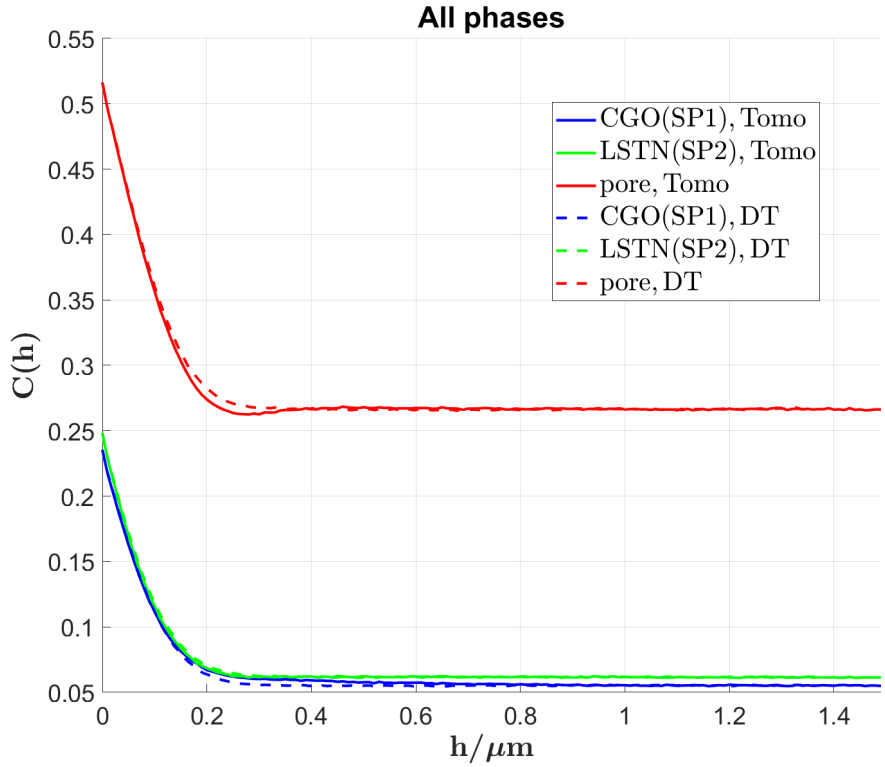

Fig. 26 Comparison of the covariance functions for the real structure from tomography (Tomo) and the digital microstructure twin (DT) for the CGO40-LSTN60 sample.

G Figure of merit for additional potential reaction sites of MIEC electrodes

As for example reported by Burnat et al.[8] for LST-CGO anodes, an additional process can be identified based on EIS-investigations, which is probably related to a reaction at the TPBs or at the surface of the titanate (i.e., pore-LSTN interface). Thus, the TPB-lengths and/or the pore-LSTN interface area might contribute to the reaction kinetics of LSTN-CGO anodes. However, this contribution can be expected to be inferior compared to the reaction related to the pore-CGO interface area (see also discussion in the main article. Nevertheless, the corresponding figures of merit shall be reported here. It must be emphasized that these expressions indicate the regions where the additional reaction sites might show a relevant contribution, but not directly represent the total performance of the cell.

The figure of merit for a potential contribution of the pore-LSTN interface area can be formulated as follows:

$$ASR^{-1}_{\mathrm{surface,LSTN}} \propto \sqrt{\sigma_{\mathrm{rel,ion,comp}} \cdot IA_{\mathrm{V,pore-LSTN}}}, \tag{15}$$

where $\sigma_{\mathrm{rel,ion,comp}}$ is the relative ionic composite conductivity and $IA_{\mathrm{V,pore-LSTN}}$ the volume specific pore-LSTN interface area considered as the active reaction site for fuel oxidation. The corresponding contour plots of the volume specific pore-LSTN interface area and the figure of merit $ASR^{-1}_{\mathrm{surface,LSTN}}$ for the LSTN surface reaction are reported in Fig. 27 a) and b). According to this estimate, the contribution from the LSTN

surface reaction positively correlates with the total solid volume fraction ϕ_{tot}. Moreover, it is maximal for an LSTN-content of 30 % (i.e., $\phi_{\mathrm{SP1,rel}} = 70\,\%$) and decreases for lower LSTN-contents $< 30\,\%$ because of the too low LSTN-surface area and decreases for higher LSTN-contents $> 30\,\%$ because of the lower ionic composite conductivity associated with the lower CGO-content.

The figure of merit for a potential contribution of the TPBs can be formulated as follows:

$$ASR^{-1}_{\mathrm{TPB,MIEC}} \propto \sqrt{\sigma_{\mathrm{rel,ion,comp}} \cdot L_{\mathrm{V,TPB}}}, \tag{16}$$

where $\sigma_{\mathrm{rel,ion,comp}}$ is the relative ionic composite conductivity and $L_{\mathrm{V,TPB}}$ the volume specific TPB-length, which is considered as the active reaction site for fuel oxidation. The corresponding contour plots for the original TPB-length and the figure of merit for the TPB-reaction is presented in Fig. 28 a) and b). The inverse ASR positively correlates with the total solid volume fraction ϕ_{tot} and the maximal value is found for a CGO-content around $\phi_{\mathrm{SP1,rel}} = 75\,\%$. Thereby, the use of the total TPB-length seems to be appropriate for the case of MIEC composite electrodes. Due to the MIEC properties of both phases, no disconnected regions are expected. In contrast, for common composite anodes like Ni-YSZ, the transport of ions is restricted to the YSZ-phase and thus, only the contiguous TPBs (Fig. 28 c)) and the single-phase conductivity of the ion conducting phase are relevant for the reaction. The corresponding contour plot of $ASR^{-1}_{\mathrm{TPB,MIEC}}$ reported in Fig. 28 d) positively correlates with the total solid volume fraction ϕ_{tot} and the maximal value is again found for a CGO-content around $\phi_{\mathrm{SP1,rel}} = 75\,\%$. However, the region with high values is considerably more confined near $\phi_{\mathrm{SP1,rel}} = 75\,\%$, as the contiguous TPB-length (see Fig. 28 c)) decreases significantly stronger towards low volume fraction of one of the solid phases compared to the total TPB-length (see Fig. 28 a)). Moreover, the performance practically vanishes for CGO-contents below 20 %, because the CGO-phase drops below the percolation threshold (see Fig. 11 c) of the main article). In contrast, a minimal performance remains for $ASR^{-1}_{\mathrm{TPB,MIEC}}$, as the used composite conductivity is insensitive to a percolation loss of one of the solid phases. The figures of merit $ASR^{-1}_{\mathrm{TPB,MIEC}}$ and $ASR^{-1}_{\mathrm{TPB,cont}}$ are also reported for the PGM-NW dataset in Fig. 15 b) and d) of section E. Even if the principal behaviour is similar, the comparison reveals a quantitatively different and more complex behaviour of the DT-dataset compared to the PGM-NW dataset for this performance indicators. These results confirm that the appropriate representation of the wetting behaviour of the solid phases and the optimization of the relative conductivities with morphological operations, as performed for the DT-dataset, are essential in order to obtain a realistic representation and variation of the electrode microstructure.

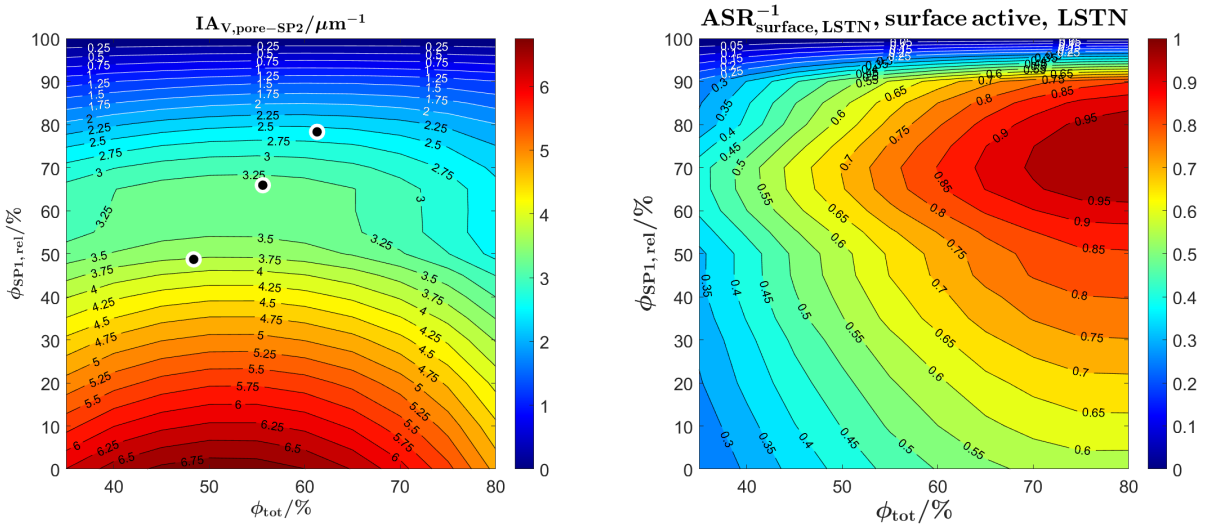

(a) Volume specific interface area pore-LSTN $IA_{\mathrm{V,pore-LSTN}}$

(b) Surface active electrode, LSTN: $ASR^{-1}_{\mathrm{surface,LSTN}} \propto \sqrt{\sigma_{\mathrm{rel,ion,comp}} \cdot IA_{\mathrm{V,pore-LSTN}}}$ (see Eq. 15)

Fig. 27 Figures of merit for the contribution of the surface reaction on LSTN assuming that the transport of gas species and the transport of electrons is not limiting. Contour plots of a) pore-LSTN interface area and b) figure of merit $ASR^{-1}_{\mathrm{surface,LSTN}}$ normalized to values between 0-1 as a function of the total solid volume fraction ϕ_{tot} (i.e., 100 % - porosity, respectively) and the relative volume fraction of CGO $\phi_{\mathrm{SP1,rel}}$ (composition).

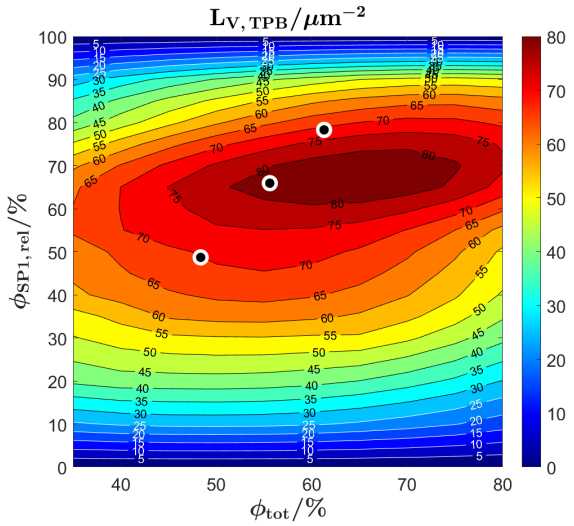

(a) Volume specific the three-phase boundary length $L_{V,TPB}$

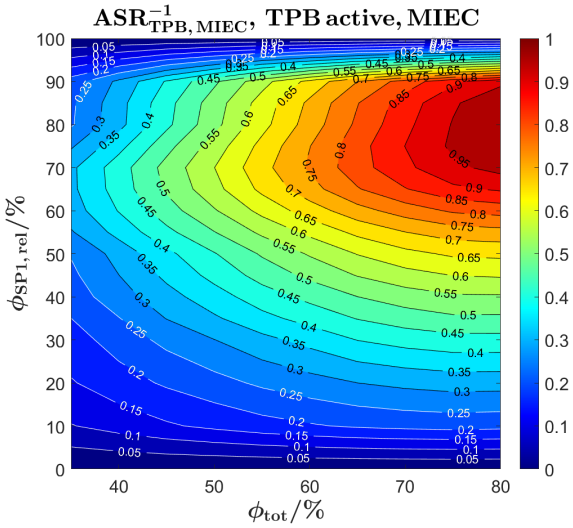

(b) TPB active MIEC electrode: $ASR^{-1}_{TPB,MIEC} \propto \sqrt{\sigma_{rel,ion,comp} \cdot L_{V,TPB}}$ (see Eq. 16)

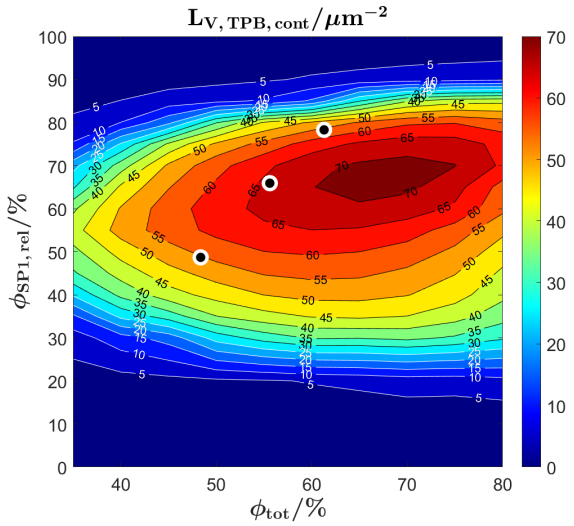

(c) Contiguous volume specific the three-phase boundary length $L_{V,TPB,cont}$

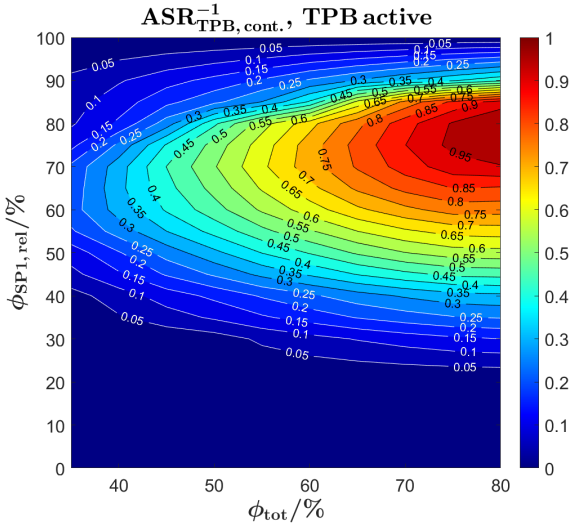

(d) Classical contiguous TPB active electrode (e.g., Ni-YSZ): $ASR^{-1}_{TPB,cont.} \propto \sqrt{\sigma_{rel,SP1} \cdot L_{V,TPB,cont}}$ (see Eq. 11 in the main article.)

Fig. 28 Figures of merit for the electrode performance assuming that the transport of gas species and the transport of electrons is not limiting. The corresponding contour plots are shown as a function of the total solid volume fraction ϕ_{tot} (i.e., 100% - porosity, respectively) and the relative volume fraction of CGO $\phi_{SP1,rel}$ (composition) for b) a TPB active MIEC electrode and d) a classical TPB active electrodes (e.g., Ni-YSZ). Note that the data is normalized to values between 0-1. The corresponding contour plots of the original and contiguous volume specific TPB-lengths are shown in a) and c), respectively.

References

1 B. Abdallah, F. Willot and D. Jeulin, *Journal of Microscopy*, 2016.

2 P. Marmet, L. Holzer, T. Hocker, G. K. Boiger, H. Bausinger, A. Mai, M. Fingerle, S. Reeb, D. Michel and J. M. Brader, *Energy Advances*, 2023, **2**, 980 – 1013.

3 Math2Market GmbH, *GeoDict simulation software Release 2022*, 2022, doi.org/10.30423/release.geodict2022.

4 P. Marmet, *PhD thesis, Digital Materials Design of Solid Oxide Fuel Cell Anodes*, University of Fribourg, Switzerland, 2023.

5 P. Marmet, L. Holzer, J. G. Grolig, H. Bausinger, A. Mai, J. M. Brader and T. Hocker, *Physical Chemistry Chemical Physics*, 2021, **23**, 23042–23074.

6 S. B. Adler, *Journal of The Electrochemical Society*, 1996, **143**, 3554–3564.
7 MathWorks, *MATLAB*, 2021, `https://mathworks.com/`.
8 D. Burnat, G. Nasdaurk, L. Holzer, M. Kopecki and A. Heel, *Journal of Power Sources*, 2018, **385**, 62–75.